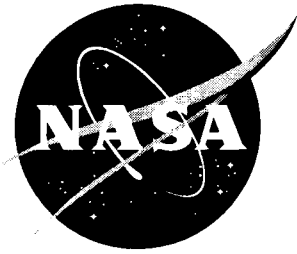


NASA/TM-2003-212412



Effect of Turbulence Models on Two Massively-Separated Benchmark Flow Cases

*Christopher L. Rumsey
Langley Research Center, Hampton, Virginia*

May 2003

The NASA STI Program Office . . . in Profile

Since its founding, NASA has been dedicated to the advancement of aeronautics and space science. The NASA Scientific and Technical Information (STI) Program Office plays a key part in helping NASA maintain this important role.

The NASA STI Program Office is operated by Langley Research Center, the lead center for NASA's scientific and technical information. The NASA STI Program Office provides access to the NASA STI Database, the largest collection of aeronautical and space science STI in the world. The Program Office is also NASA's institutional mechanism for disseminating the results of its research and development activities. These results are published by NASA in the NASA STI Report Series, which includes the following report types:

- **TECHNICAL PUBLICATION.** Reports of completed research or a major significant phase of research that present the results of NASA programs and include extensive data or theoretical analysis. Includes compilations of significant scientific and technical data and information deemed to be of continuing reference value. NASA counterpart of peer-reviewed formal professional papers, but having less stringent limitations on manuscript length and extent of graphic presentations.
- **TECHNICAL MEMORANDUM.** Scientific and technical findings that are preliminary or of specialized interest, e.g., quick release reports, working papers, and bibliographies that contain minimal annotation. Does not contain extensive analysis.
- **CONTRACTOR REPORT.** Scientific and technical findings by NASA-sponsored contractors and grantees.

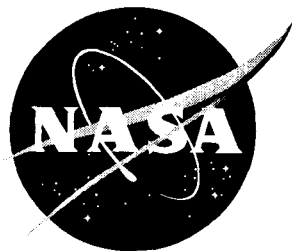
- **CONFERENCE PUBLICATION.** Collected papers from scientific and technical conferences, symposia, seminars, or other meetings sponsored or co-sponsored by NASA.
- **SPECIAL PUBLICATION.** Scientific, technical, or historical information from NASA programs, projects, and missions, often concerned with subjects having substantial public interest.
- **TECHNICAL TRANSLATION.** English-language translations of foreign scientific and technical material pertinent to NASA's mission.

Specialized services that complement the STI Program Office's diverse offerings include creating custom thesauri, building customized databases, organizing and publishing research results ... even providing videos.

For more information about the NASA STI Program Office, see the following:

- Access the NASA STI Program Home Page at <http://www.sti.nasa.gov>
- E-mail your question via the Internet to help@sti.nasa.gov
- Fax your question to the NASA STI Help Desk at (301) 621-0134
- Phone the NASA STI Help Desk at (301) 621-0390
- Write to:
NASA STI Help Desk
NASA Center for Aerospace Information
7121 Standard Drive
Hanover, MD 21076-1320

NASA/TM-2003-212412



Effect of Turbulence Models on Two Massively-Separated Benchmark Flow Cases

Christopher L. Rumsey
Langley Research Center, Hampton, Virginia

National Aeronautics and
Space Administration

Langley Research Center
Hampton, Virginia 23681-2199

May 2003

Available from:

NASA Center for AeroSpace Information (CASI)
7121 Standard Drive
Hanover, MD 21076-1320
(301) 621-0390

National Technical Information Service (NTIS)
5285 Port Royal Road
Springfield, VA 22161-2171
(703) 605-6000

Contents

ABSTRACT	iv
1 INTRODUCTION	1
2 NUMERICAL METHOD	1
3 EXPLICIT ALGEBRAIC STRESS MODELS	2
4 SPECIFICS OF THE TWO CASES	4
4.1 2-D Hill	4
4.2 Ahmed Body	5
5 RESULTS	6
5.1 2-D Hill	6
5.2 Ahmed Body	8
6 CONCLUSIONS	10
ACKNOWLEDGMENTS	10

ABSTRACT

Two massively-separated flow cases (the 2-D hill and the 3-D Ahmed body) were computed with several different turbulence models in the Reynolds-averaged Navier-Stokes code CFL3D as part of participation in a turbulence modeling workshop held in Poitiers, France in October, 2002. Overall, results were disappointing, but were consistent with results from other RANS codes and other turbulence models at the workshop. For the 2-D hill case, those turbulence models that predicted separation location accurately ended up yielding a too-long separation extent downstream. The one model that predicted a shorter separation extent in better agreement with LES data did so only by coincidence: its prediction of earlier reattachment was due to a too-late prediction of the separation location. For the Ahmed body, two slant angles were computed, and CFD performed fairly well for one of the cases (the larger slant angle). Both turbulence models tested in this case were very similar to each other. For the smaller slant angle, CFD predicted massive separation, whereas the experiment showed reattachment about half-way down the center of the face. These test cases serve as reminders that state-of-the-art CFD is currently not a reliable predictor of massively-separated flow physics, and that further validation studies in this area would be beneficial.

1 INTRODUCTION

Computational fluid dynamics (CFD) codes using the Reynolds-averaged Navier-Stokes (RANS) equations are now used routinely for complex aerodynamic flows. CFD is often trusted for many attached flow situations, but the same cannot be said for configurations with significant regions of separation. In general, CFD has not reliably predicted a wide enough variety of separated flows accurately to earn the users' trust in these situations.

Engineers do not agree on the cause for disagreements between CFD and separated flow experiments. Some of the cause may be that current turbulence models (or the RANS assumptions inherent in the models) are unable to handle some of the complex, unsteady physics involved. But it is also more difficult to obtain reliable experimental data at these conditions, so some of the fault may be attributed to difficulty in using CFD to model precisely the same problem as the experiment. In particular, it is certainly dubious whether a truly two-dimensional experiment involving separated flow could ever be attained. As a result, 2-D CFD validations and comparisons are suspect.

Therefore, it continues to be a valuable exercise to test different existing turbulence models on as wide a variety of separated flow cases as possible. Each case teaches us more about the potential limitations of RANS and existing turbulence models on different classes of separated flows, and also helps to point out potential pitfalls inherent in the process of comparing CFD with experiment.

The European Research Community On Flow, Turbulence and Combustion (ERCOFTAC) has been instrumental in organizing many validation workshops for the purpose of furthering the understanding of CFD's capabilities and limitations for different classes of flows. A workshop on refined Turbulence Modeling (10th joint ERCOFTAC (SIG-15) / IAHR / QNET-CFD) was held in October 2002 in Poitiers, France, and featured three flows: contra-rotating jets, periodic flow over a 2-D hill, and flow over a simplified car body (Ahmed body).

This report details contributions to the latter two of these cases, using the NASA code CFL3D [1]. Several different turbulence models were employed, and results were compared to large-eddy simulation (LES) results in the case of the 2-D hill, and to experiment in the case of the Ahmed body.

The next two sections describe the CFL3D computer code and the formulas for the explicit algebraic stress models (EASM) (the other turbulence models employed are more widely used and are available in the open literature, so they are not described in this document). Then, the specifics of two test cases are given, the results are described, and conclusions are drawn.

2 NUMERICAL METHOD

The computer code CFL3D [1] solves the three-dimensional, time-dependent, Reynolds averaged compressible Navier-Stokes equations with an upwind finite-volume formulation (it can also be exercised in two-dimensional mode of operation for 2-D cases). It can solve flows over multiple-zone grids that are connected in a one-to-one, patched, or overset manner, and can employ grid sequencing, multigrid, and local time stepping when accelerating convergence to steady state. Upwind-biased spatial differencing is used for the inviscid terms, and flux limiting is used to obtain smooth solutions in the vicinity of shock waves, when present. Viscous terms are centrally differenced, and cross-diffusion terms are neglected. For very low Mach number flows,

preconditioning [2] is used to insure convergence and accuracy of the solutions.

The CFL3D code is advanced in time with an implicit approximate factorization method. The implicit derivatives are written as spatially first-order accurate, which results in block tridiagonal inversions for each sweep. However, for solutions that utilize Roe flux-difference splitting [3], the block tridiagonal inversions are further simplified using a diagonal algorithm with a spectral radius scaling of the viscous terms.

The turbulence models are solved uncoupled from the mean flow equations using implicit approximate factorization. Their advective terms are solved using first-order upwind differencing. Many turbulence models are available in CFL3D, but only those used in the current study are mentioned here. Descriptions of the one-equation Spalart-Allmaras (SA) and the two-equation Menter $k-\omega$ shear-stress transport (SST) turbulence models can be found in their respective references [4, 5], while a more detailed description of the EASM is given in the next section.

3 EXPLICIT ALGEBRAIC STRESS MODELS

The turbulent stress tensor for EASM is given by

$$\begin{aligned} \tau_{ij} = & \frac{2}{3} K \delta_{ij} - 2\nu_t^* (S_{ij} \\ & + [a_2 a_4 (S_{ik} W_{kj} - W_{ik} S_{kj}) \\ & - 2a_3 a_4 (S_{ik} S_{kj} - \frac{1}{3} S_{kl} S_{lk} \delta_{ij})]), \end{aligned} \quad (1)$$

where $S_{ij} = [(\partial u_i / \partial x_j) + (\partial u_j / \partial x_i)] / 2$ and $W_{ij} = [(\partial u_i / \partial x_j) - (\partial u_j / \partial x_i)] / 2$. The nonlinear terms are within the brackets []. The component τ_{ij} terms are used to close the Reynolds-averaged Navier-Stokes equations (see, e.g., Ref. [6]). The kinematic eddy viscosity ν_t^* is given by

$$\nu_t^* \equiv C_\mu^* K \tau = -K \alpha_1, \quad (2)$$

with $\tau \equiv 1/\omega$. Thus, α_1/τ is equivalent to $-C_\mu^*$. The value of α_1/τ is obtained from the solution to the following cubic equation at each point in the flow field:

$$\left(\frac{\alpha_1}{\tau}\right)^3 + p \left(\frac{\alpha_1}{\tau}\right)^2 + q \left(\frac{\alpha_1}{\tau}\right) + r = 0, \quad (3)$$

where

$$p = -\frac{\gamma_1^*}{\eta^2 \tau^2 \gamma_0^*} \quad (4)$$

$$\begin{aligned} q = & \frac{1}{(2\eta^2 \tau^2 \gamma_0^*)^2} (\gamma_1^{*2} - 2\eta^2 \tau^2 \gamma_0^* a_1 \\ & - \frac{2}{3} \eta^2 \tau^2 a_3^2 + 2\mathcal{R}^2 \eta^2 \tau^2 a_2^2) \end{aligned} \quad (5)$$

$$r = \frac{\gamma_1^* a_1}{(2\eta^2 \tau^2 \gamma_0^*)^2}. \quad (6)$$

The correct root to choose from this equation is the root with the lowest real part [7]. Also, the degenerate case when $\eta^2 \rightarrow 0$ must be avoided. See Rumsey and Gatski [8] for further details. In the current implementation, the resulting $C_\mu^* = -(\alpha_1/\tau)$ is limited by $C_\mu^* = \max(C_\mu^*, 0.0005)$.

The nominal level for C_μ^* in a zero-pressure-gradient log layer is approximately 0.09. Other parameters are given by

$$\eta^2 \equiv \{\mathbf{S}^2\} = S_{ij}S_{ji} = S_{ij}S_{ij} \quad (7)$$

$$\{\mathbf{W}^2\} = W_{ij}W_{ji} = -W_{ij}W_{ij} \quad (8)$$

$$\mathcal{R}^2 = -\frac{\{\mathbf{W}^2\}}{\{\mathbf{S}^2\}} \quad (9)$$

$$a_1 = \frac{1}{2} \left(\frac{4}{3} - C_2 \right) \quad (10)$$

$$a_2 = \frac{1}{2} (2 - C_4) \quad (11)$$

$$a_3 = \frac{1}{2} (2 - C_3) \quad (12)$$

$$a_4 = \left[\gamma_1^* - 2\gamma_0^* \left(\frac{\alpha_1}{\tau} \right) \eta^2 \tau^2 \right]^{-1} \tau. \quad (13)$$

Also,

$$\gamma_0^* = C_1^1/2 \quad (14)$$

$$\gamma_1^* = \frac{1}{2} C_1^0 + \left(\frac{C_{\varepsilon 2} - C_{\varepsilon 1}}{C_{\varepsilon 1} - 1} \right) \quad (15)$$

and $C_{\varepsilon 1} = 1.44$, $C_{\varepsilon 2} = 1.83$, $C_1^0 = 3.4$, $C_1^1 = 1.8$, $C_2 = 0.36$, $C_3 = 1.25$, and $C_4 = 0.4$.

The preceding implementation is exactly the same for the EASM-ko (using K - ω equations) or EASM-ke (using K - ε equations), except that $\tau \equiv K/\varepsilon$ for EASM-ke. For EASM-ko, the explicit tensor representation for τ_{ij} is coupled with the following K - ω two-equation model:

$$\frac{DK}{Dt} = \mathcal{P} - f_{\beta^*} K \omega + \frac{\partial}{\partial x_k} \left[\left(\nu + \frac{\nu_t^*}{\sigma_K} \right) \frac{\partial K}{\partial x_k} \right] \quad (16)$$

$$\frac{D\omega}{Dt} = \gamma \frac{\omega}{K} \mathcal{P} - \beta \omega^2 + \frac{\partial}{\partial x_k} \left[\left(\nu + \frac{\nu_t^*}{\sigma_\omega} \right) \frac{\partial \omega}{\partial x_k} \right], \quad (17)$$

where

$$\mathcal{P} = -\tau_{ij} \frac{\partial u_i}{\partial x_j} \approx 2\nu_t^* \eta^2 \quad (18)$$

and $\sigma_K = 1$, $\sigma_\omega = \kappa^2 / [\sqrt{C_\mu}(\beta - \gamma)]$, $\kappa = 0.41$, $\gamma = 0.53$, $\beta = 0.83$, and $C_\mu = 0.0895$. Note that for 2-D incompressible flows, $\mathcal{P} = 2\nu_t^* \eta^2$ is exact. Also, it should be noted that the values of σ_K and γ are different than reported in Rumsey and Gatski [8]. They were changed recently to improve the model's capability for jet-type flows (see Georgiadis et al.[9]). The change was found to have relatively small impact for wall-bounded flows in general. In the current implementation, \mathcal{P} in the K -equation is limited to be less than 20 times the destruction term $f_{\beta^*} K \omega$. The function f_{β^*} , taken from Wilcox [10], is given by

$$f_{\beta^*} = 1 \quad \text{when} \quad \chi_k \leq 0 \quad (19)$$

$$f_{\beta^*} = \frac{1 + 680\chi_k^2}{1 + 400\chi_k^2} \quad \text{when} \quad \chi_k > 0 \quad (20)$$

$$\chi_k = \frac{C_\mu^2}{\omega^3} \frac{\partial K}{\partial x_j} \frac{\partial \omega}{\partial x_j}, \quad (21)$$

where the C_μ^2 term in the formula for χ_k is necessary because ω in the current model does not “absorb” C_μ as in Wilcox’s model.

For the EASM-ke two-equation model:

$$\frac{DK}{Dt} = \mathcal{P} - \varepsilon + \frac{\partial}{\partial x_k} \left[\left(\nu + \frac{\nu_t}{\sigma_K} \right) \frac{\partial K}{\partial x_k} \right] \quad (22)$$

$$\frac{D\varepsilon}{Dt} = C_{\varepsilon 1} \frac{\varepsilon}{K} \mathcal{P} - f_\varepsilon C_{\varepsilon 2} \frac{\varepsilon^2}{K} + \frac{\partial}{\partial x_k} \left[\left(\nu + \frac{\nu_t}{\sigma_\varepsilon} \right) \frac{\partial \varepsilon}{\partial x_k} \right], \quad (23)$$

where $f_\varepsilon = [1 - \exp(-Re_K/10.8)]$, $Re_K = K^{1/2}d/\nu$, $\sigma_K = 1.0$, $\sigma_\varepsilon = \kappa^2/[\sqrt{C_\mu}(C_{\varepsilon 2} - C_{\varepsilon 1})]$, $C_{\varepsilon 1} = 1.44$, $C_{\varepsilon 2} = 1.83$, $C_\mu = 0.0885$, and d is the distance to the nearest wall. Additional wall damping functions (such as f_μ , to achieve expected asymptotic behavior of the turbulence quantities very near the wall) are not employed in the current model. Note that in equations (22) and (23), the diffusion terms are modeled using an *equilibrium* eddy viscosity $\nu_t = C_\mu K^2/\varepsilon$, where the constant $C_\mu = 0.0885$ for this model. This is different than in the EASM-ko model, which uses the *actual* eddy viscosity ν_t^* (with variable C_μ^*) in its modeled diffusion terms. The diffusion terms for both EASM-ko and EASM-ke are approximate models in any case; see, for example, Warsi [11].

The turbulent boundary conditions applied at solid walls are $K_w = 0$, $\varepsilon_w = 2\nu_w(\partial\sqrt{K}/\partial n)_w^2$, and $\omega_w = 10(6\nu_w)/[\beta(\Delta n)^2]$, where Δn is the distance to the first cell center away from the wall. The boundary condition for ω_w is from Menter [5]. This boundary condition simulates the analytical behavior of ω near solid walls without the need for specifying the solution at interior points.

4 SPECIFICS OF THE TWO CASES

4.1 2-D Hill

The 2-D hill case was originally an experiment reported by Almeida et al.[12], but some modifications were made to the geometry and test conditions for the purpose of conducting a CFD analysis using LES by Jang et al.[13]. It was subsequently decided to use this 3-D LES simulation as the reference by which the 2-D RANS models were judged in the Poitiers workshop.

To simulate incompressible flow in the CFL3D compressible CFD code, the Mach number for the 2-D hill case was set very low ($M=0.001$), and preconditioning was employed. The Reynolds number was 10595 per hill height H . For boundary conditions, the lower and upper walls were solid (viscous, adiabatic). Turbulence equations were integrated all the way to the walls. The minimum normal spacing at the lower wall ensured an average minimum y^+ of approximately 0.25 for the finest grid, 0.5 on the medium grid, and 1.1 on the coarse grid. The outflow boundary condition set $p/p_{\text{ref}} = 1.0$ and extrapolated density and velocity from the interior. The subsonic inflow boundary specified density, velocity profiles, and turbulence quantity profiles (appropriate to each particular turbulence model) from the LES data, and extrapolated pressure from the interior.

Two hills were included in the computational domain. The distance between hills peaks was $9H$, and the upper wall was $3.035H$ above the lower wall. The grid extended from $x/H=-3$ upstream to $x/H=15$ downstream, with some opening-up of the grid in the streamwise direction near the outflow boundary. The finest-level grid employed 737 streamwise points and 193 normal

points. There was grid stretching in the normal direction in order to give appropriate minimum spacings near each wall (the minimum spacing near the upper wall was larger than that at the lower wall: on the fine grid, average minimum y^+ for the upper wall was 1.7 while on the lower wall it was 0.25). Fig. 1 shows a picture of the grid, with every fourth gridpoint shown in both coordinate directions for clarity.

The shape of each hill (which is symmetric about its peak at $x = 0$) is described by the following equations, given in mm (the hill height H in these equations is 28 mm, so they describe the shape of the hill between $x/H=0$ and 1.9286):

$$y(x) = \min(28., 28. + .0067751 * x^2 - .0021245 * x^3) \quad \text{when} \quad 0 \leq x \leq 9 \quad (24)$$

$$y(x) = 25.074 + .97548 * x - .10161 * x^2 + .0018898 * x^3 \quad \text{when} \quad 9 \leq x \leq 14 \quad (25)$$

$$y(x) = 25.796 + .82067 * x - .090554 * x^2 + .0016265 * x^3 \quad \text{when} \quad 14 \leq x \leq 20 \quad (26)$$

$$y(x) = 40.464 - 1.3796 * x + .019459 * x^2 - .00020703 * x^3 \quad \text{when} \quad 20 \leq x \leq 30 \quad (27)$$

$$y(x) = 17.925 + .87439 * x - .055674 * x^2 + .00062777 * x^3 \quad \text{when} \quad 30 \leq x \leq 40 \quad (28)$$

$$y(x) = \max(0., 56.390 - 2.0105 * x + .016449 * x^2 + .000026750 * x^3) \quad \text{when} \quad 40 \leq x \leq 54 \quad (29)$$

4.2 Ahmed Body

The Ahmed body experimental data is from Lienhart et al.[14], although the first experimental studies on this configuration were carried out by Ahmed and Ramm [15]. The Ahmed body is a simplified car shape with a hatch-back. Different slant angles for the hatch-back have been tested. Although geometrically very simple, the flow around this body is similar in many respects to the flow around a real automobile. During testing, the body was elevated off the floor using stilts, so there is an underbody flow as well. A sketch of the model, taken from Manceau and Bonnet [16], is shown in Fig. 2.

The flow conditions were: $M = 0.117$, $Re = 2667$ per mm. Only one half of the body was simulated (a symmetry plane was employed along the centerline of the body). A farfield (Riemann-invariant) boundary condition was employed in the far field. This “open” type of far field conditions was found by Durand et al.[17] to yield improved inlet velocity profiles over “closed” boundary conditions (for which the farfield boundaries above and to the side of the body are modeled as solid slip walls). The body and the tunnel floor were solid (viscous, adiabatic). Turbulence equations were integrated all the way to these surfaces. The average minimum y^+ at all solid walls was approximately 1.5.

The grids were obtained from CFX, a supplier of computational fluid dynamics software and service (Durand et al.[17]). Only two slant angles were considered: 25° and 35° . In both cases the stilts beneath the body were ignored. For the 25° slant angle case, the grid contained 1.3×10^6 gridpoints. For the 35° slant angle case, the grid contained 1.25×10^6 gridpoints. Each grid was a multi-zone grid (29 zones) with 1-to-1 connectivity between the zones. In the current study, no grid sensitivity analysis was performed. However, Durand et al.[17] did perform such a study. Based on their analysis, the current grid sizes (considered “medium” level) were deemed sufficiently fine for turbulence model analysis.

In the grids, the distance from the leading edge of the car to the inflow plane of the grid was 2100 mm, and the distance from the back of the car to the outflow plane of the grid was 5220 mm (the length of the car was 1044 mm). The body height was 288 mm. Its bottom was 50 mm above the floor, and the total grid height from the floor was 1206 mm (1062 mm from the top of the car). The car half-width was 194.5 mm, and the total grid width from the center plane was 935 mm (740.5 mm from the side of the car). Two views of the 35° grid are shown in Figs. 3 and 4. Although not shown, the 25° case has similar features.

5 RESULTS

5.1 2-D Hill

For the 2-D hill computations, the inflow profiles were set to approximately match the LES data, as shown in Fig. 5. Note that all quantities have been nondimensionalized by the bulk velocity U_b above the hill peak at $x/H=0$. A grid study was conducted using the EASM-ke model, using the finest 737×193 grid level as well as 3 additional coarser levels, obtained by successively removing every other gridpoint from the finer grid. Sample results are given in Fig. 6, at the sensitive region $x/H=2$ (in the separated region behind the hill). The u -velocity, the turbulent kinetic energy k , and the turbulent shear stress uv each shows only small variations between the two finest grid levels, indicating that the 369×97 and the 737×193 are both sufficient to capture these quantities to plotting accuracy. The v -velocity shows noticeable variations even between the two finest grid levels, indicating that the 369×97 is not fine enough to adequately capture this quantity, and the 737×193 may or may not be fine enough (an even finer grid would be needed to establish its adequacy). However, in this study a finer grid was not attempted, and the 737×193 grid was assumed to be sufficient and was used for all computations to be presented below.

From the grid density study using the EASM-ke model, the separation location (at $x/H=0.343$ on the finest grid) converges in a second-order fashion as the grid is refined (there is a linear variation with the inverse of the total number of gridpoints N , which is proportional to the square of the average grid spacing), consistent with second-order global spatial accuracy of CFL3D. See Fig. 7. Using extrapolation, the separation point on an infinitely-refined grid would be approximately $x/H=0.340$.

However, the reattachment location (at $x/H=3.704$ on the finest grid) is not converging in a second-order fashion as the grid is refined. See Fig. 8. Apparently, all three of the finest grid levels do not lie within the “asymptotic range” for this variable, which means that even finer grids would be needed to establish the second-order property of the reattachment point. Thus, the best that can be said using the current grid levels is that the reattachment point on an infinitely-refined grid would likely be somewhere in the range of $x/H=3.75$ to 3.9 for EASM-ke.

Table 1: Summary of 2-D hill computed separation and reattachment locations

Model	Sep pt.	Reattach pt.
SA	0.207	7.685
SST	0.203	7.648
EASM-ke	0.343	3.704
EASM-ko	0.254	7.461
LES (reference)	0.22	4.72

In summary, using the finest 737×193 grid, the separation point is definitively captured to within less than 1%, and the reattachment point is likely captured to within approximately 5%.

In the 3-D LES computation used as reference [13] (which had a spanwise extent of $4.5H$ and used periodic boundary conditions in that direction), the flow was unsteady and contained significant spanwise three-dimensional structures. On the average, the flow separated at $x/H=0.22$, and reattached at $x/H=4.72$, although the time-dependent variations in these locations was quite large. The goal for this test case was to try to determine what turbulence model, if any, best mimics the averaged LES data in the 2-D sense.

A summary of the computed separation and reattachment points for all the turbulence models used in this study is given in Table 1.

Results using the SA model are shown in Figs. 9 and 10. Streamlines are plotted in Fig. 11. The SA model separates at $x/H=0.207$, in reasonable agreement with the LES data, but it reattaches at $x/H=7.685$, far downstream of where the LES reattaches on average. In general, the u -velocity profiles are predicted in good agreement with LES through the separation location to about $x/H=2 - 3$; beyond this point the SA model continues to predict separated flow well past where the LES reattaches. The peak turbulent shear stress is underpredicted in magnitude by SA at all stations, and fails to replicate the profile shape at $x/H=0.05$.

Results using the SST model are shown in Figs. 12, 13, and 14. Streamlines are plotted in Fig. 15. The SST model's velocity and turbulent shear stress profiles, separation and reattachment points are very similar to those of SA. The turbulent kinetic energy profiles (which were not plotted for SA because that model is a one-equation model and does not provide that quantity) are generally underpredicted in magnitude compared to the LES data.

Results using the EASM-ke model are shown in Figs. 16, 17, and 18. Streamlines are plotted in Fig. 19. The velocity profiles overall agree fairly well with the LES data, particularly downstream of $x/H=4$. However, EASM-ke separates at $x/H=0.343$, significantly downstream of the LES results. Overall, the EASM-ke turbulent shear stress levels generally underpredict LES, similar to SA and SST. But at $x/H=7$, the computed turbulent shear stress values agree with the LES, then at $x/H=8$ they exceed LES in magnitude. The peak k is generally underpredicted at most x -locations.

Results using the EASM-ko model are shown in Figs. 20, 21, and 22. Streamlines are plotted in Fig. 23. Results are generally similar to SA and SST regarding separation and reattachment, although the separation point is slightly downstream and reattachment slightly upstream. Regarding turbulent shear stress and turbulent kinetic energy profiles, results are similar in character to the other models, in that they generally underpredict the peak levels compared to LES.

For this case, it is also instructive to look at the detailed budgets from the turbulence transport equations. (One of the advantages of using LES as the reference data is that it is easy to obtain these types of quantities for comparison.) Results for LES at $x/H=0.05$ (upstream of the separation location) are shown in Fig. 24, while results using three of the models are shown in Figs. 25, 26, and 27. Results using SA are not given because that model is a one-equation model and it is not clear how to extract the same variables for a direct one-on-one comparison. It should also be noted that the turbulence models used in this study did not possess pressure-diffusion or pressure-strain terms, whereas these terms could be computed from the LES.

None of the turbulence models agree very well with LES at $x/H=0.05$, although SST and EASM-ko come the closest in predicting the overall character. EASM-ke, on the other hand, predicts production term and dissipation term much too high in magnitude, with peaks too close to the wall, compared to LES. Furthermore, EASM-ke predicts turbulent diffusion and viscous diffusion terms that are too high near the wall. Given that EASM-ke did the worst job predicting separation, it is not surprising that its turbulence budget levels are the furthest in error at this station.

Results at the station $x/H=4$ are given in Figs. 28, 29, 30, and 31. This station is immediately upstream of the location in LES where reattachment occurs. As can be seen, all three turbulence models actually predict a budget very similar to LES at this location (although EASM-ke yields slightly lower peaks that are located closer to the wall than the other models). This overall agreement suggests that the turbulence models themselves are generally capturing the physics here (in the 2-D sense). Thus, the turbulence equations may already be performing as well as can be expected in the separated flow region, and it may be the lack of a 3-D mechanism in the 2-D computations that prevent SST and EASM-ko from reattaching as early as the LES. (EASM-ke *does* reattach early, but for the wrong reasons, as discussed above: it separated late.)

To summarize the 2-D hill results: SA, SST and EASM-ko each did the best job predicting the onset of separation (between $x/H=0.20 - 0.25$), in good agreement with the LES results, but then did a poor job predicting the separation length (it was greatly overpredicted). EASM-ke predicted the separation onset too late (near $x/H=0.34$), but it then predicted a more reasonable reattachment location and velocity profiles in the reattachment region. Note that it was shown in Rumsey and Gatski [8] that EASM-ke is ill-suited to predict wall-bounded adverse pressure gradient flows, so it is not surprising that it predicted separation too late.

A similar conclusion was also reached at the workshop in Poitiers: 2-D RANS turbulence models that tended to predict the “best” separation extent compared with experiment, did so only because of the fact that they predicted separation too late. For this case, there is obviously some question as to whether the simulation of unsteady 3-D structures is necessary to predict the physics of this massively-separated flow field (particularly reattachment), once it has separated at the correct location.

5.2 Ahmed Body

Two different slant angles were computed for the Ahmed body case: 25° and 35° . These two angles were chosen for the workshop because they bracket a “critical angle” at which the drag coefficient undergoes an abrupt decrease due to massively-separated flow occurring within the wake of the slant part. The crucial question for the workshop was: can RANS predict the different flow fields over the slant part at the two different slant angles? For the current study,

only the two turbulence models SST and EASM-ko were used.

Before describing results for the two different cases, boundary layer profiles are shown near mid-body, as an indication that the flowfield is being adequately predicted prior to reaching the back end of the body. The flow field in this region is not noticeably affected by the slant angle, so only results for the slant angle of 35° are shown for both turbulence models. Several u -velocity plots are shown in Figs. 32, 33, and 34. Then the U_{rms} is shown in Figs. 35, 36, and 37, where $U_{rms} = u' = \sqrt{\tau_{11}/\rho}$. The reference locations for the profiles in these figures can be found in Fig. 2.

Overall, the u -velocity profiles are in good agreement with experiment, with the exception of location C (down) on the bottom outside edge of the body, where the velocity is overpredicted. This difference is likely due to the fact that the stilts have been neglected in the computations. The U_{rms} profiles also show general agreement everywhere except at location C (down), although the “freestream” levels at location F (side) are considerably higher in the experiment than in the CFD. The two turbulence models show some differences between them, but for the most part these differences are small and both agree equally well with experiment.

In the experiment, the 25° case displayed considerable three-dimensional behavior on the slant part of the body. An open separation bubble was present on the upper part of the slant, with attached flow on the lower part, and two counter-rotating lateral vortices on the edges of the slant generated a detachment node on the side. On the other hand, the 35° case displayed essentially two-dimensional behavior. The flow separated at the top of the slant and remained separated over the entire surface.

Computed u -velocity profiles along the centerline of the 25° slant are shown in Fig. 38 for SST and EASM-ko. Corresponding $u'w'$ turbulent shear stresses are shown in Fig. 39. Both turbulence models do a very poor job predicting this flow field. Although both models predict separation just past the top of the slant, as in the experiment, neither predicts the same reattachment seen in the experiment. In fact, the CFD predicts massive separation over most of the slant surface. The $u'w'$ profiles are underpredicted in magnitude over most of the slant surface. Computed streamlines over the 25° slant surface are shown for SST and EASM-ko in Figs. 40 and 41. These figures show half of the slant face (results are symmetric about the centerline). The streamwise (+x) direction is from top to bottom, so both figures indicate that the slant face is mostly separated, although there is a pronounced region for SST near the outside bottom part of the slant where the flow has turned around. The corresponding oil/soot streak flow visualization from the experiment is shown in Fig. 42. In the experiment, the flow separates in the middle part of the top edge, but it subsequently reattaches about halfway down the face. It is clear that the CFD is not mimicking the experimental pattern.

Additional visualizations of the computed flowfield in the region of the 25° slant are shown in Figs. 43 and 44. Here, vorticity contours in three x =constant planes over the slant as well as streamlines are shown. A strong edge vortex can be seen near the side edge of the slant, and a separated shear layer exists above most of the slant face. The shape of this shear layer is different for the two turbulence models: it is somewhat curved for SST and relatively flat for EASM-ko.

Next, results for the 35° slant are presented. Computed u -velocity profiles along the centerline of the 35° slant are shown in Fig. 45. Corresponding $u'w'$ turbulent shear stresses are shown in Fig. 46. In this case, both turbulence models do a good job predicting the fully-separated nature of this flowfield. There are no significant differences between results for the two turbulence models. Computed streamlines over the 35° slant surface are shown for SST and EASM-ko

in Figs. 47 and 48. Both models produce very similar streamline patterns, although the SST model reattaches slightly further upstream on the slant than EASM-ko. The corresponding oil/soot streak flow visualization from the experiment is shown in Fig. 49. The 2-D nature of the separation is evident in this case.

Additional visualizations of the computed flowfield in the region of the 35° slant are shown in Figs. 50 and 51. In this case, the separated shear layer above the slant face is flat for both turbulence models, and lies at a higher distance above the surface than for the 25° slant case.

To summarize the Ahmed body results: SST and EASM-ko each did a poor job predicting the flow for the 25° slant, but each predicted the 35° slant fairly well. The 25° case was supposed to possess a significant region of reattached flow on the slant face, but both turbulence models predicted massive separation regardless of the slant angle. The drag coefficients predicted were: $C_{D,SST,25} = 0.311$, $C_{D,EASM-ko,25} = 0.270$, $C_{D,SST,35} = 0.297$, $C_{D,EASM-ko,35} = 0.271$. These can be compared with the experimentally-measured values of $C_{D,exp,25} = 0.285$ and $C_{D,exp,35} = 0.260$, although as much as 10% of the experimental drag values may be attributed to drag on the stilts [17].

6 CONCLUSIONS

In conclusion, two massively-separated flow cases were run with several different turbulence models in a RANS CFD code. Overall, results were disappointing, but were consistent with results from other RANS codes and other turbulence models at the ERCOFTAC turbulence modeling workshop. For the 2-D hill case, those turbulence models that predicted separation location accurately ended up yielding a too-long separation extent downstream. Only one model yielded a separation extent in reasonable agreement with the LES reference data, but this better prediction was only due to the fact that the separation location was predicted incorrectly. For the Ahmed body, two slant angles were computed, and CFD performed fairly well for one of the cases (the larger slant angle). Both turbulence models tested were very similar to each other. For the smaller slant angle, CFD predicted massive separation, whereas the experiment showed reattachment about half-way down the center of the face.

These test cases serve as reminders that state-of-the-art CFD is currently not a reliable predictor of massively-separated flow physics. Although CFD can sometimes give a reasonable indication of separated flow features and trends between different configurations, it can also sometimes yield incorrect results. This field of study would therefore benefit from continued efforts to document CFD's capabilities on a wide variety of different separated flow cases, as well as from further efforts to improve turbulence models specifically for this class of flows.

ACKNOWLEDGMENTS

The author gratefully acknowledges Dr. Martin Kuntz and Dr. Florian Menter of CFX-Germany for making available their grids for the Ahmed body.

References

- [1] Krist, S. L., Biedron, R. T., and Rumsey, C. L., "CFL3D User's Manual (Version 5.0)," NASA TM-1998-208444, June 1998.
- [2] Weiss, J. M., and Smith, W. A., "Preconditioning Applied to Variable and Constant Density Flows," *AIAA Journal*, Vol. 33, No. 11, 1995, pp. 2050-2057.
- [3] Roe, P. L., "Approximate Riemann Solvers, Parameter Vectors, and Difference Schemes," *J. Computational Physics*, Vol. 43, 1981, pp. 357-372.
- [4] Spalart, P. R., and Allmaras, S. R., "A One-Equation Turbulence Model for Aerodynamic Flows," *La Recherche Aerospatiale*, No. 1, 1994, pp. 5-21.
- [5] Menter, F. R., "Two-Equation Eddy-Viscosity Turbulence Models for Engineering Applications," *AIAA Journal*, Vol. 32, No. 8, 1994, pp. 1598-1605.
- [6] Gatski, T. B., "Turbulent Flows: Model Equations and Solution Methodology," *Handbook of Computational Fluid Mechanics*, edited by R. Peyret, Academic Press, London, 1996, pp. 339-415.
- [7] Jongen, T., and Gatski, T. B., "A Unified Analysis of Planar Homogeneous Turbulence Using Single-Point Closure Equations," *Journal of Fluid Mechanics*, Vol. 399, 1999, pp. 117-150.
- [8] Rumsey, C. L., and Gatski, T. B., "Recent Turbulence Model Advances Applied to Multi-element Airfoil Computations," *J. Aircraft*, Vol. 38, No. 5, 2001, pp. 904-910.
- [9] Georgiadis, N. J., Rumsey, C. L., Yoder, D. A., and Zaman, K. B. M. Q., "Effects of RANS Turbulence Modeling on Calculation of Lobed Nozzle Flowfields," AIAA Paper 2003-1271, January 2003.
- [10] Wilcox, D. W., *Turbulence Modeling For CFD*, 2nd ed., DCW Industries, La Canada, 1998.
- [11] Warsi, Z. U. A., *Fluid Dynamics, Theoretical and Computational Approaches*, CRC Press, Inc., Boca Raton, 1993, pp. 544-454.
- [12] Almeida, G. P., Durao, D. F. G., and Heitor, M. V., "Wake Flows Behind Two Dimensional Model Hills," *Exp. Thermal and Fluid Science*, Vol. 7, 1993, pp. 87-101.
- [13] Jang, Y. J., Temmerman, L., and Leschziner, M. A., "Investigation of Anisotropy-Resolving Turbulence Models by Reference to Highly-Resolved LES Data for Separated Flows," EC-COMAS Computational Fluid Dynamics Conference 2001, Swansea, Wales.
- [14] Lienhart, H., Stoots, C., and Becker, S., "Flow and Turbulence Structures in the Wake of a Simplified Car Model (Ahmed Model)," DGLR Fach Symp. der STAB, Stuttgart Univ., Nov. 15-17, 2000.
- [15] Ahmed, S. R. and Ramm, G., "Some Salient Features of the Time-Averaged Ground Vehicle Wake," SAE Technical Paper 840300, 1984.
- [16] Manceau, R. and Bonnet, J.-P., "10th joint ERCOFTAC (SIG-15) -IAHR-QNET/CFD Workshop on Refined Turbulence Modelling," <<http://labo.univ-poitiers.fr/informations-lea/Workshop-Ercoftac-2002/Index.html>>, 2002.

- [17] Durand, L., Kuntz, M., and Menter, F., “Validation of CFX-5 for the Ahmed Car Body,” CFX validation report, CFX-VAL13/1002, 2002.

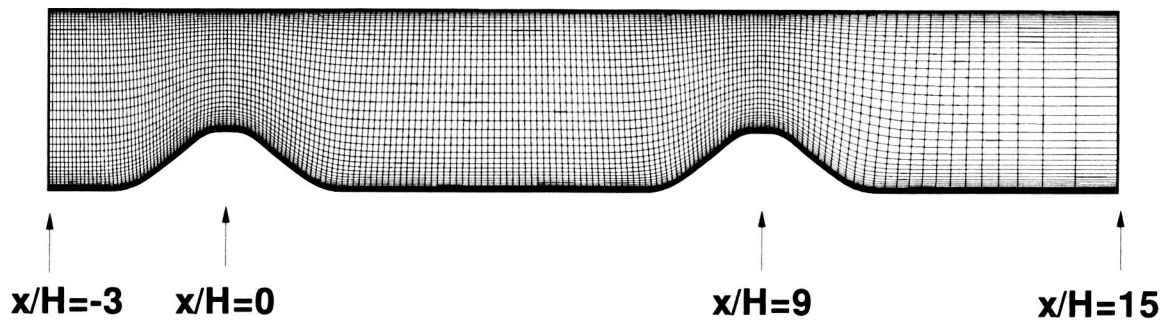
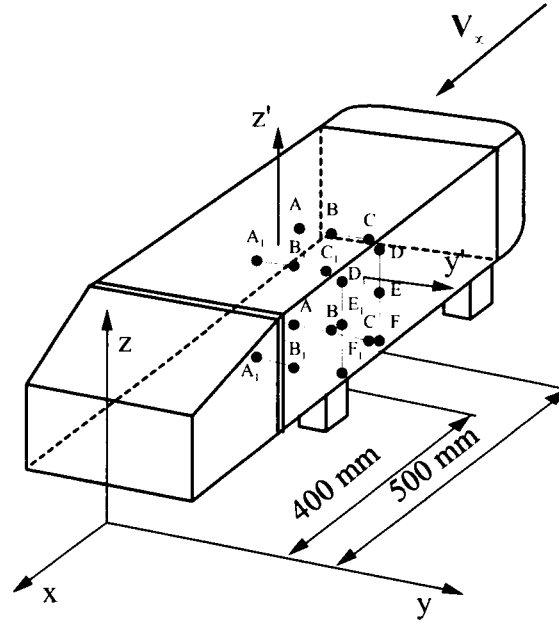


Figure 1: 2-D hill grid, with every fourth gridpoint shown.



Top	x	y
A	-500	0
A ₁	-400	0
B	-500	80
B ₁	-400	80
C	-500	160
C ₁	-400	160

Side	x	z
D	-500	294
D ₁	-400	294
E	-500	194
E ₁	-400	194
F	-500	94
F ₁	-400	94

Down	x	y
A	-500	0
A ₁	-400	0
B	-500	80
B ₁	-400	80
C	-500	160

Figure 2: Sketch of the model showing locations of boundary layer measurements on the central part of the body (from Manceau and Bonnet [16]).

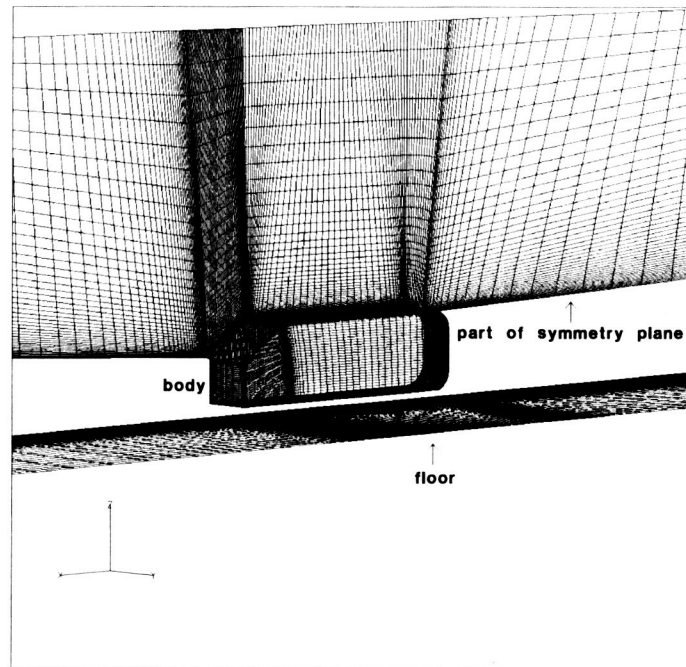


Figure 3: View of the 35° grid, from the side (flow is from right to left).

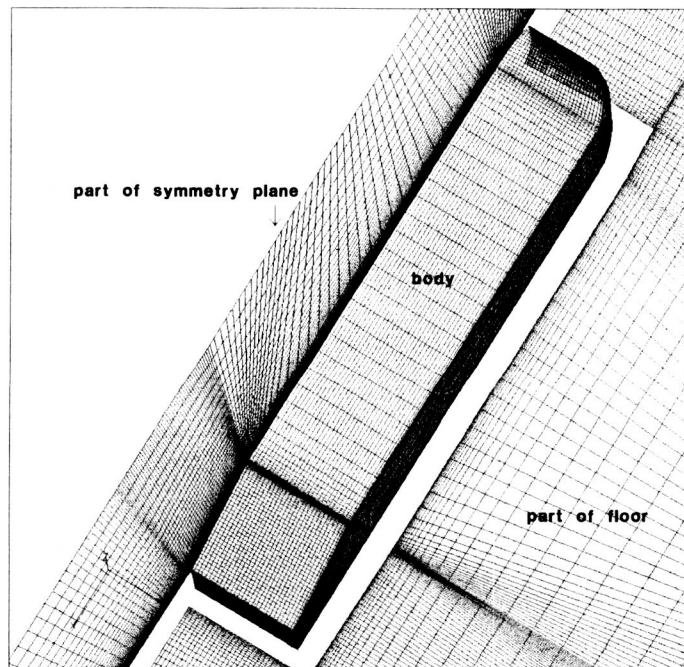


Figure 4: View of the 35° grid, from the top (flow is from top to bottom).

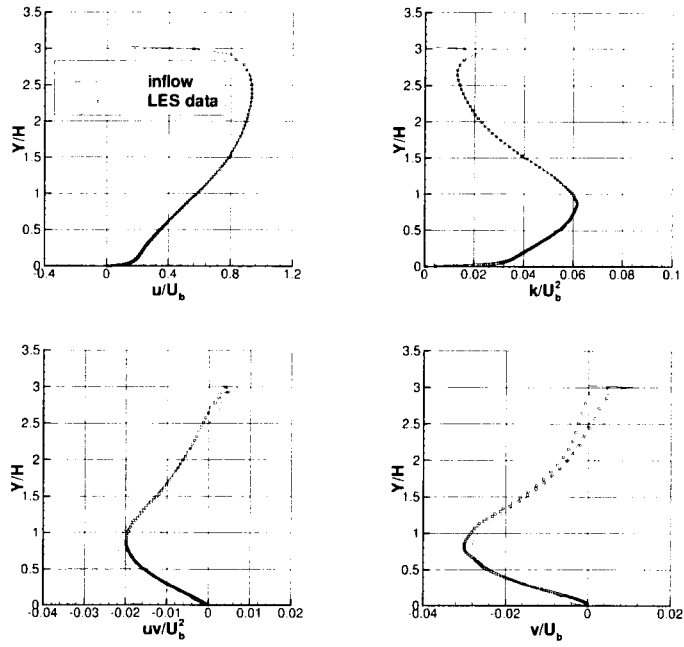


Figure 5: Inflow profiles specified in the 2-D hill computations.

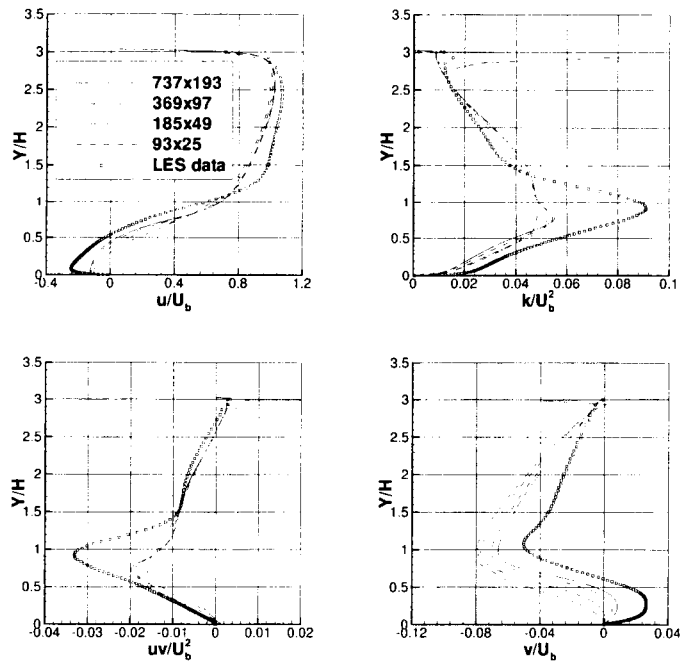


Figure 6: 2-D hill grid study using EASM-ke at $x/H=2$.

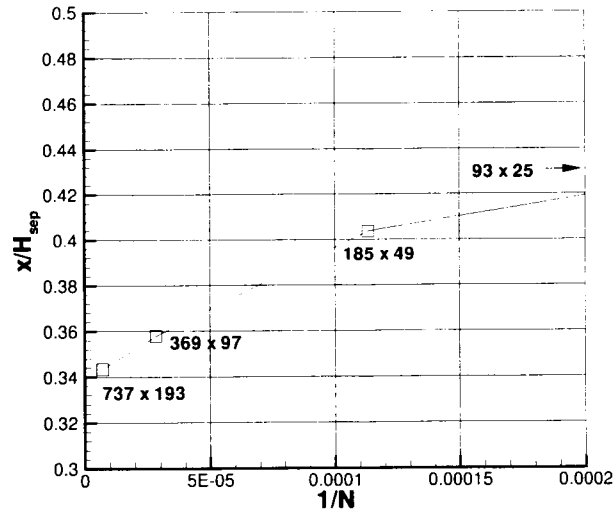


Figure 7: 2-D hill grid study showing computed separation location as the grid is refined using EASM-ke.

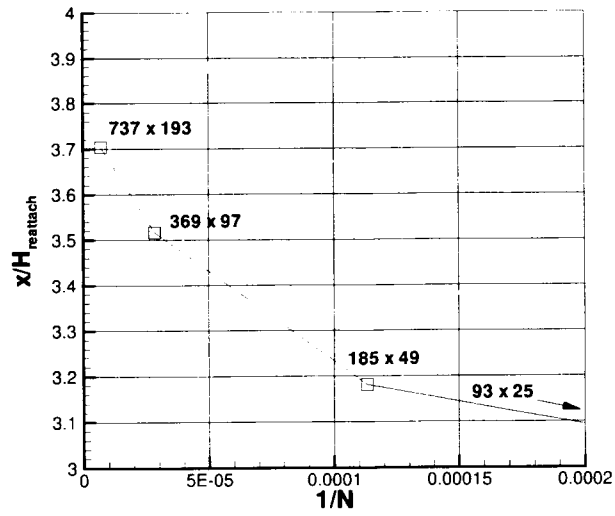


Figure 8: 2-D hill grid study showing computed reattachment location as the grid is refined using EASM-ke.

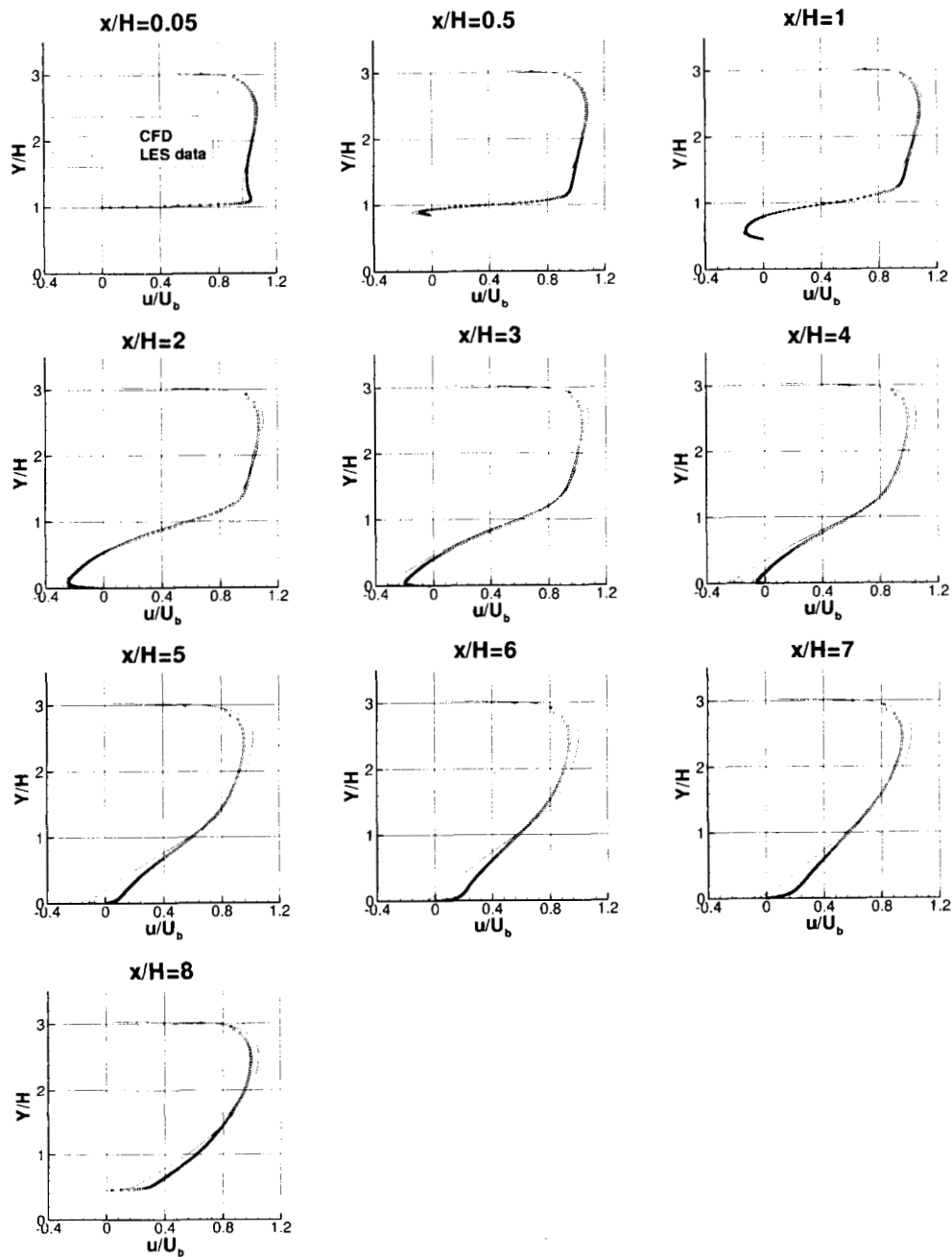


Figure 9: Velocity profiles for 2-D hill using SA, 737×193 grid.

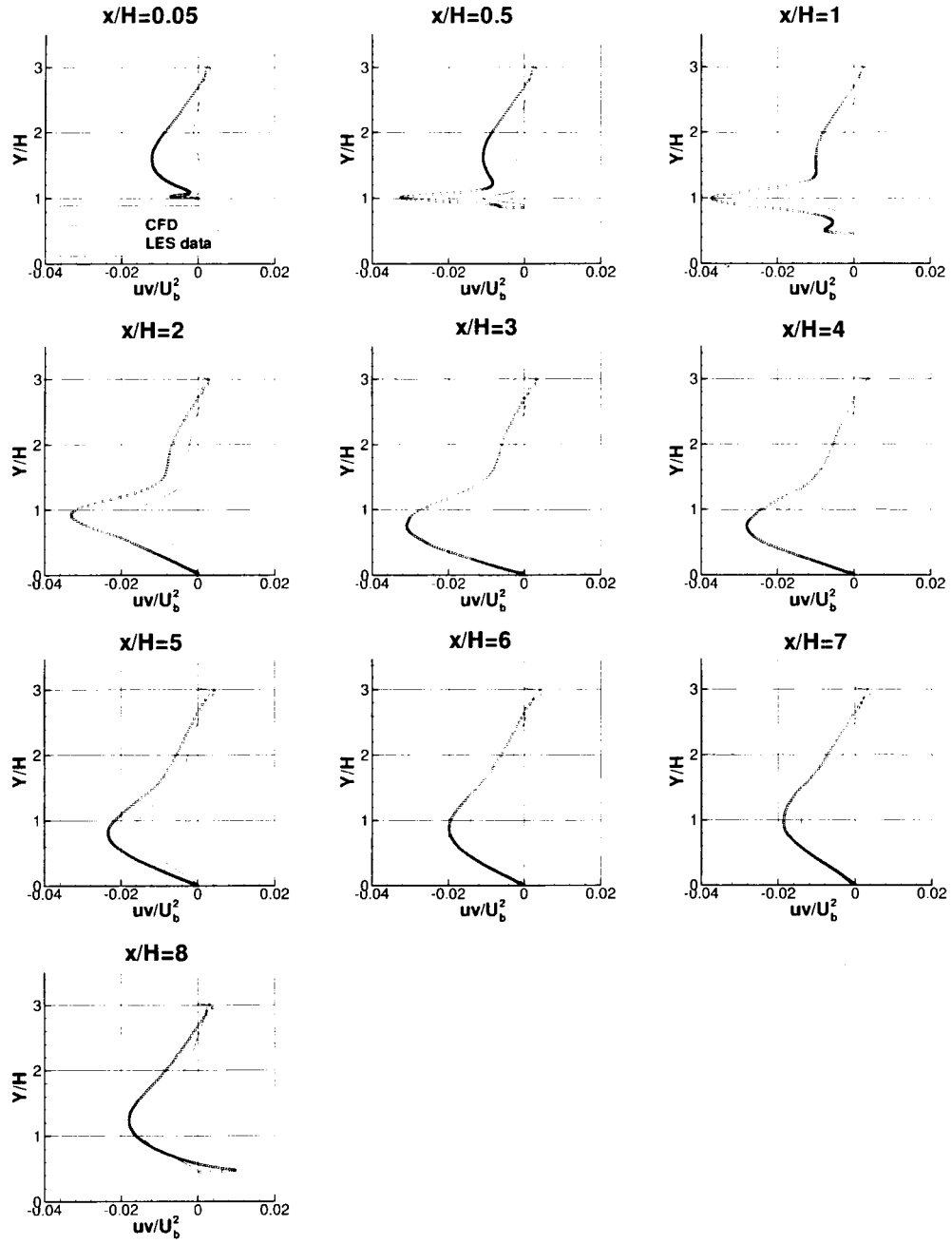


Figure 10: Turbulent shear stress profiles for 2-D hill using SA, 737×193 grid.

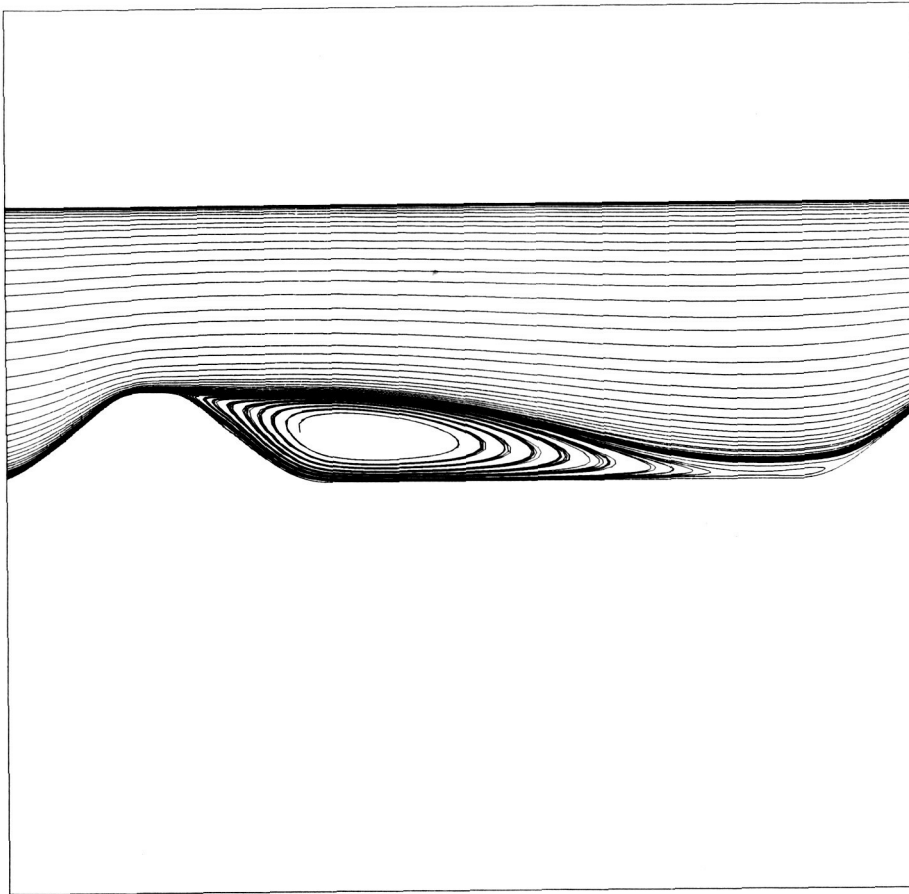


Figure 11: Streamlines for 2-D hill using SA, 737×193 grid.

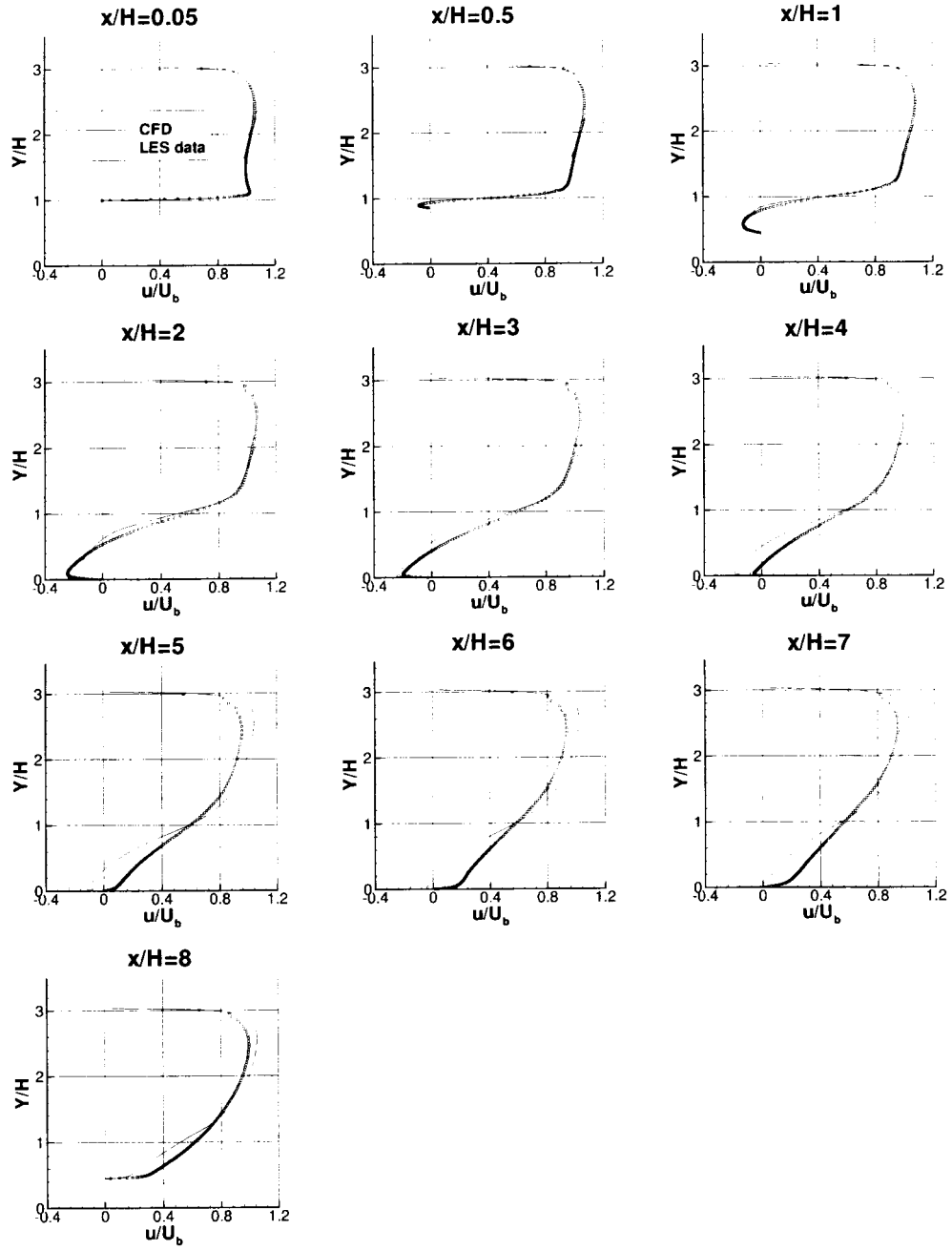


Figure 12: Velocity profiles for 2-D hill using SST, 737×193 grid.

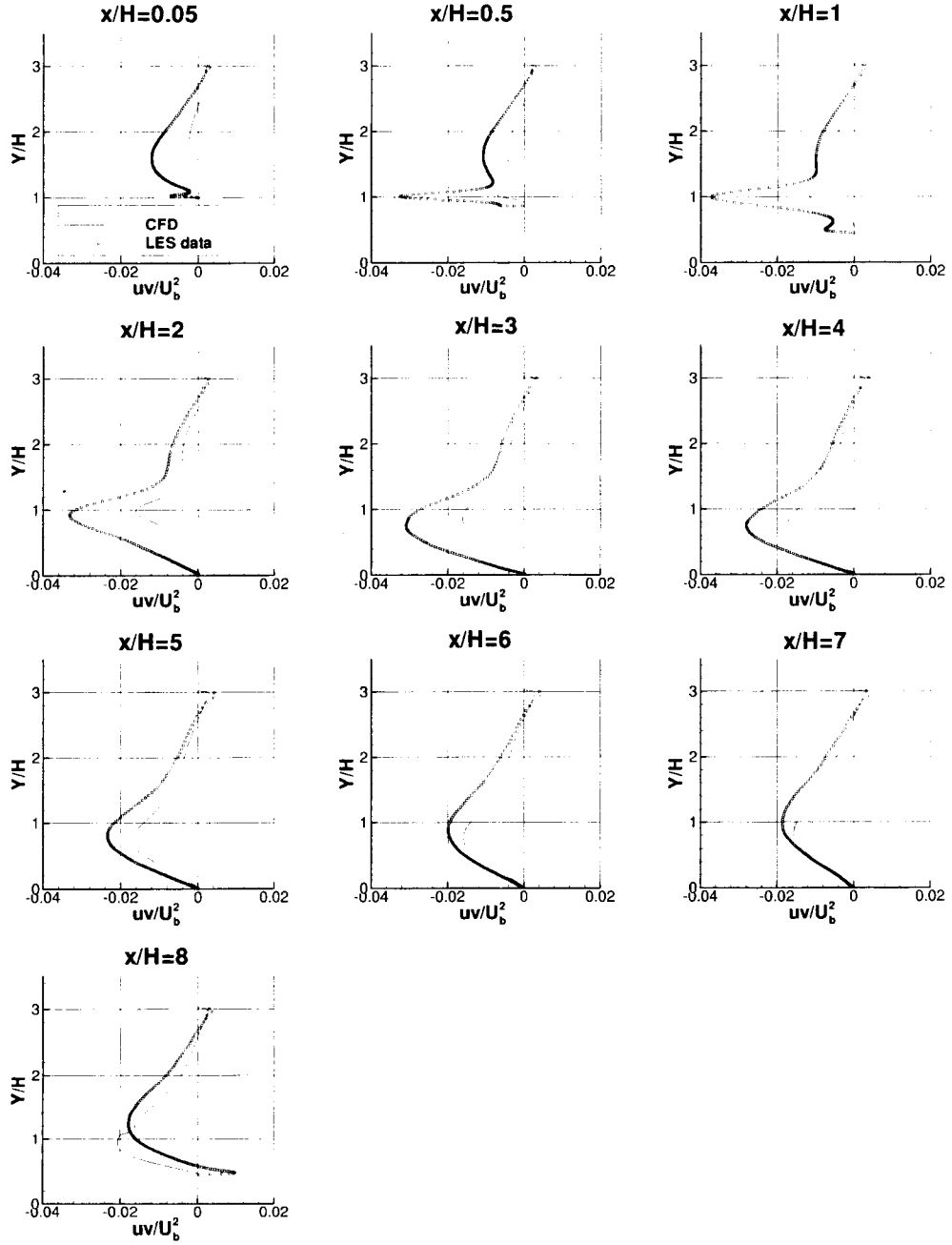


Figure 13: Turbulent shear stress profiles for 2-D hill using SST, 737 \times 193 grid.

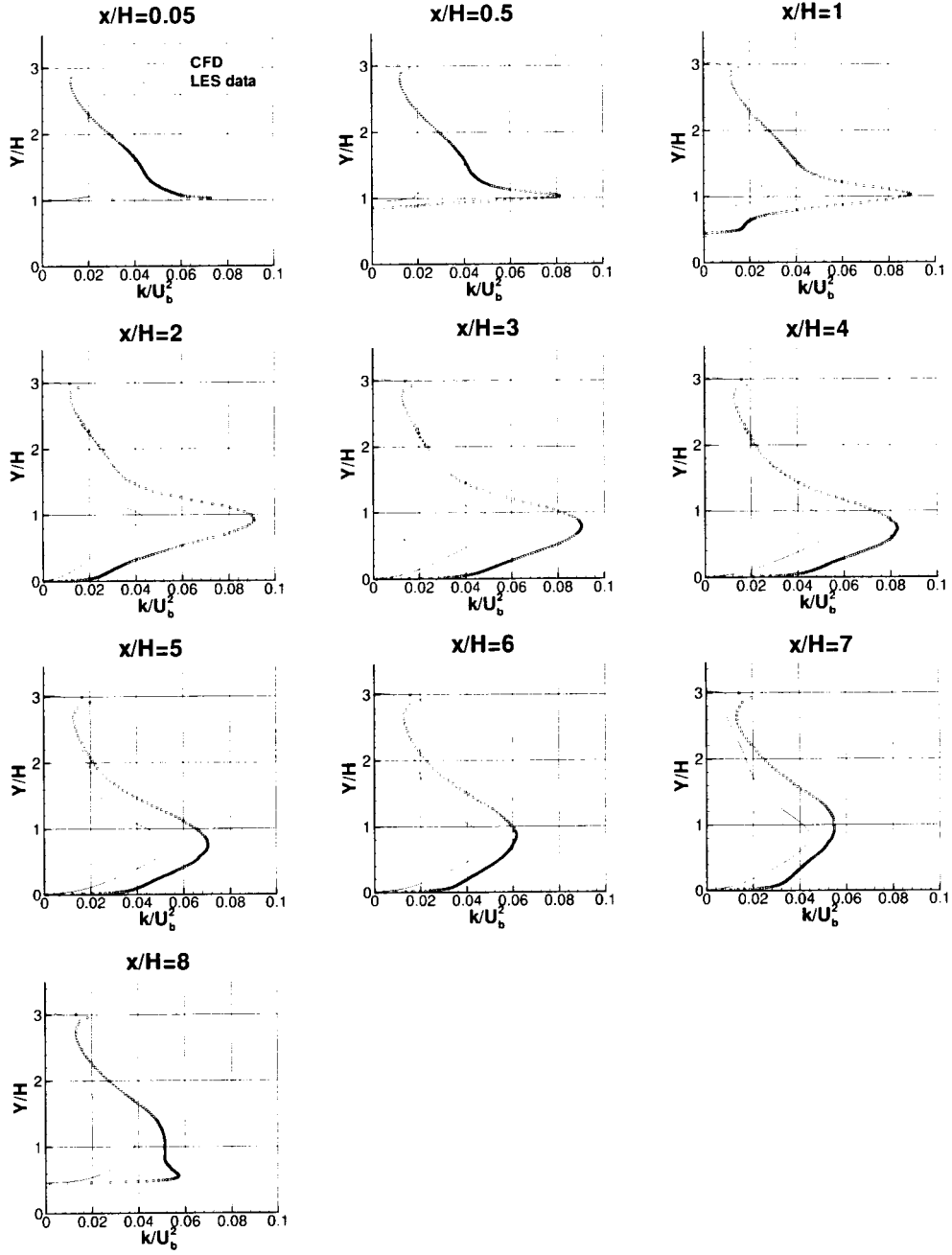


Figure 14: Turbulent kinetic energy profiles for 2-D hill using SST, 737×193 grid.

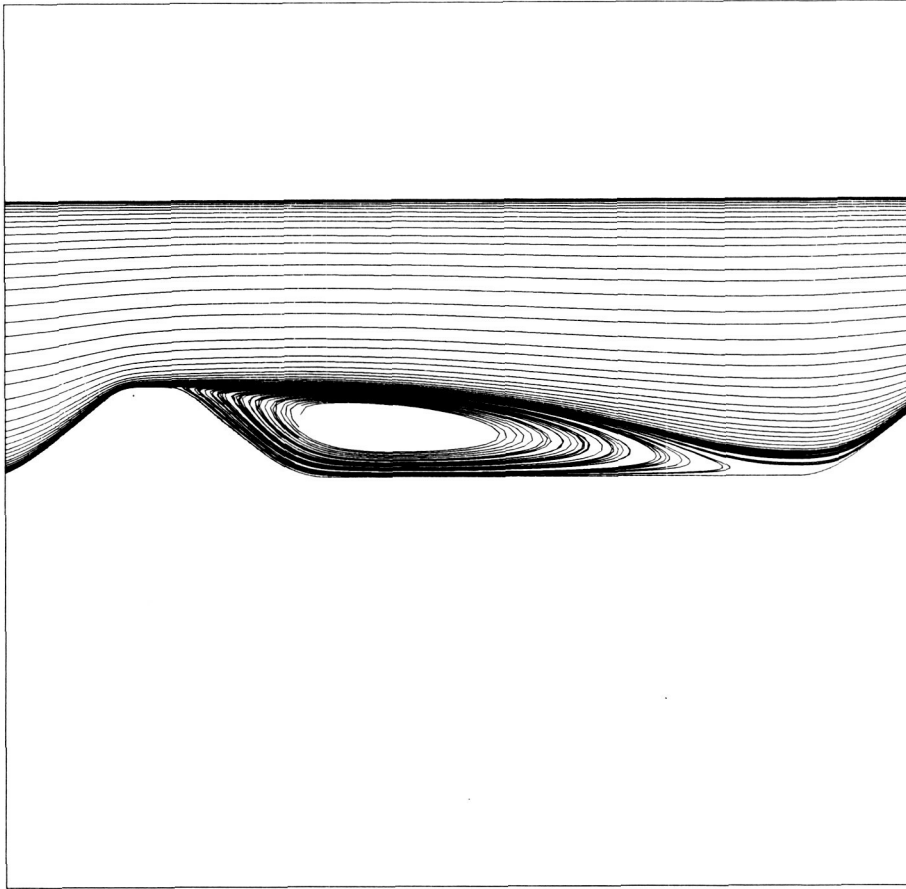


Figure 15: Streamlines for 2-D hill using SST, 737×193 grid.

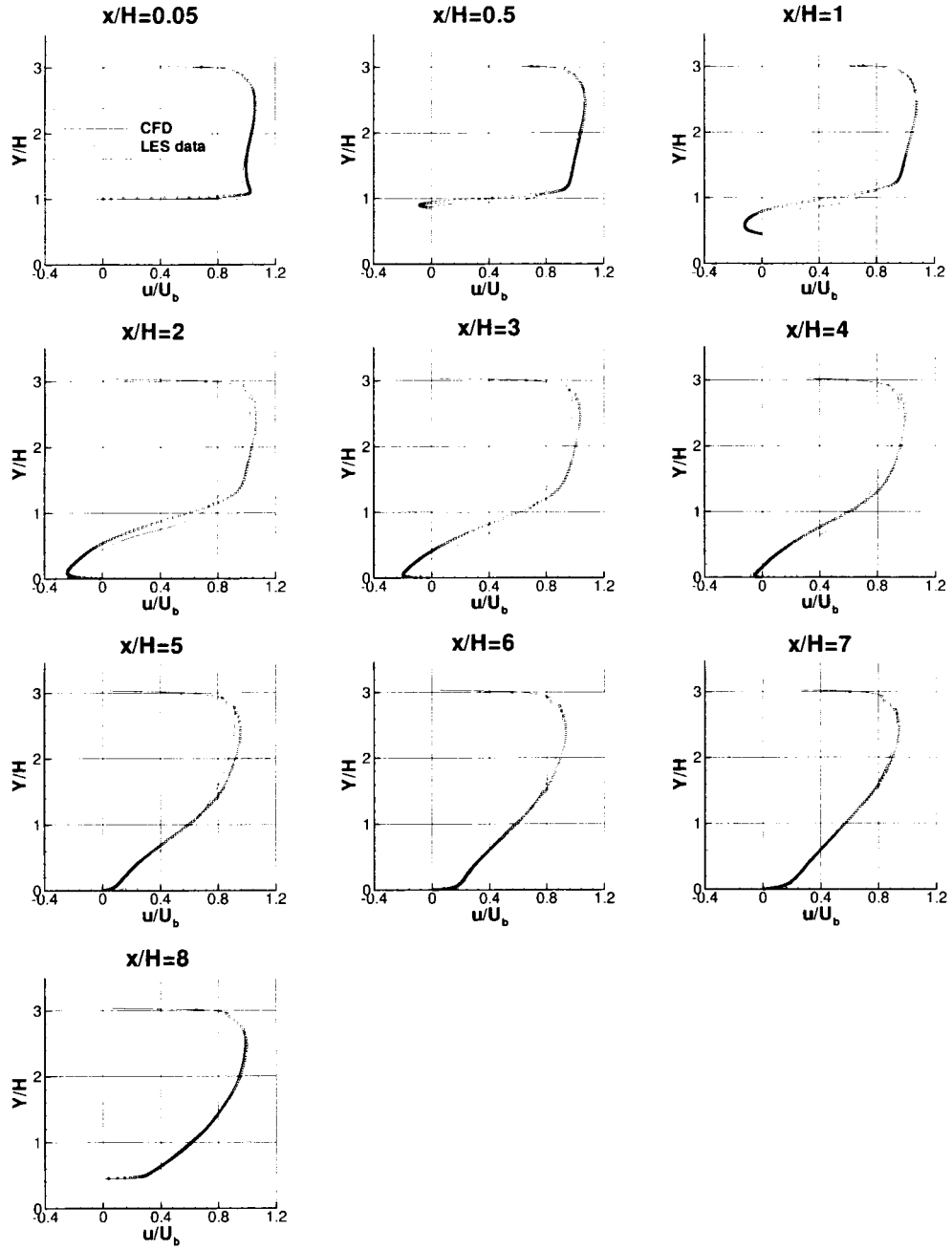


Figure 16: Velocity profiles for 2-D hill using EASM-ke, 737×193 grid.

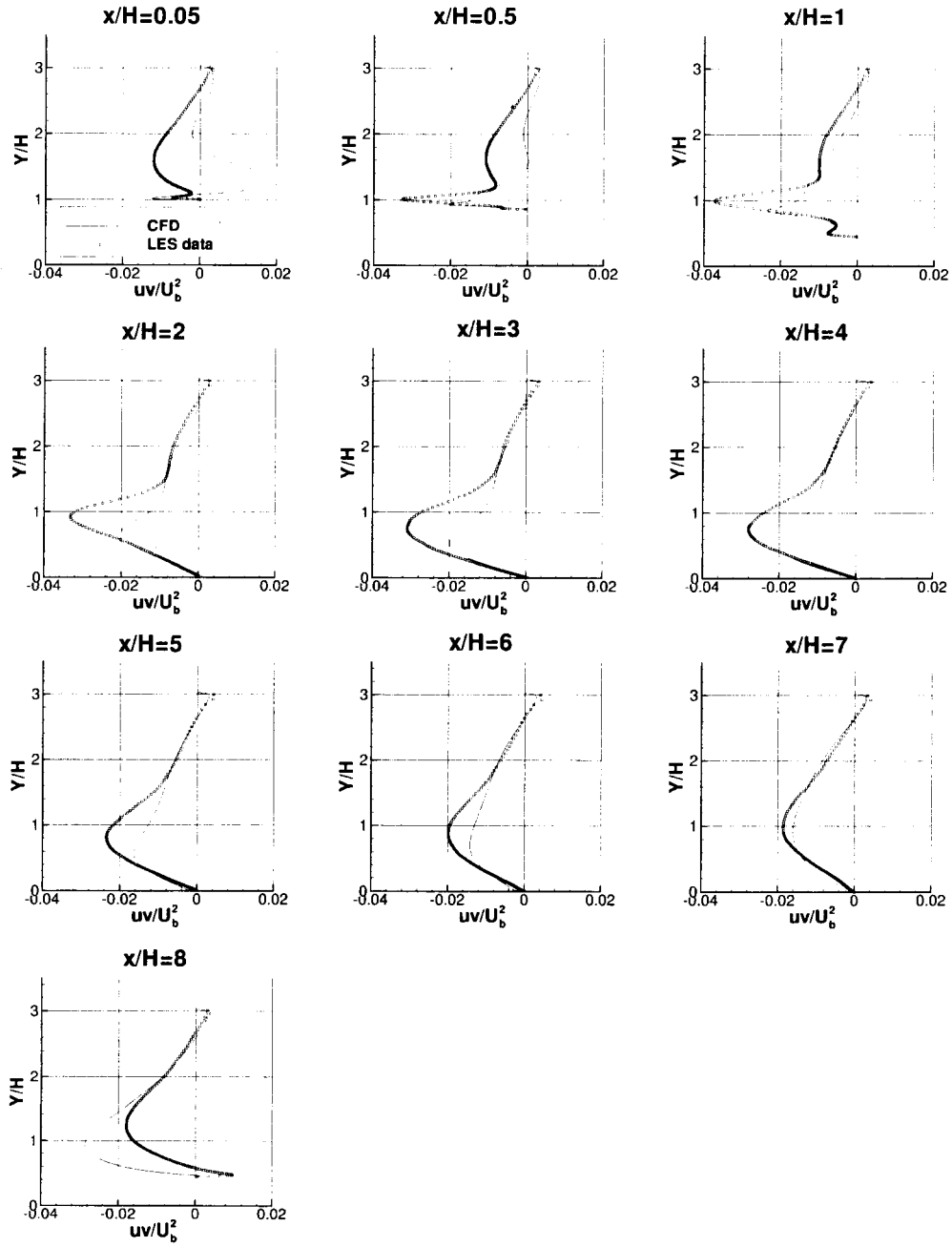


Figure 17: Turbulent shear stress profiles for 2-D hill using EASM-ke, 737×193 grid.

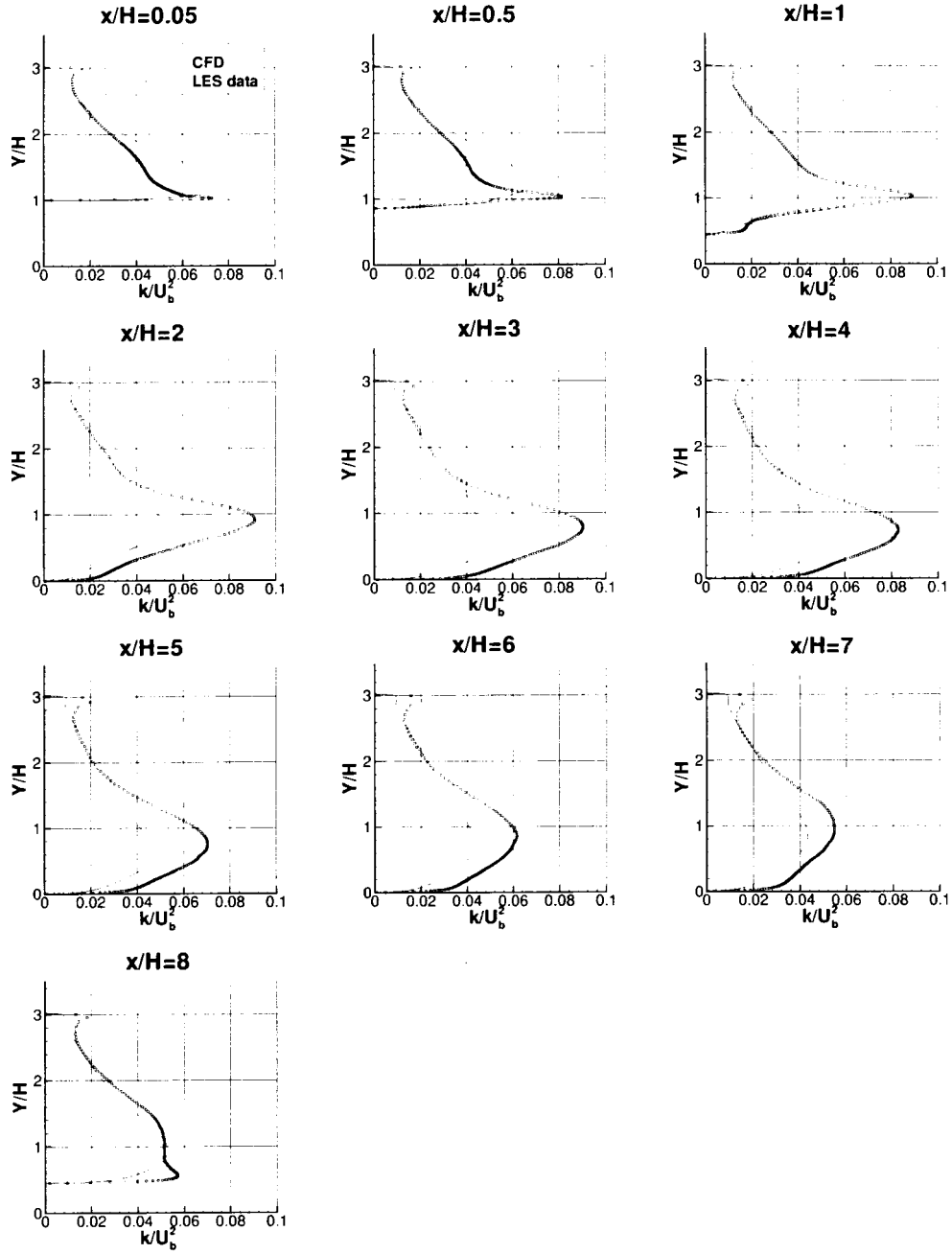


Figure 18: Turbulent kinetic energy profiles for 2-D hill using EASM-ke, 737×193 grid.

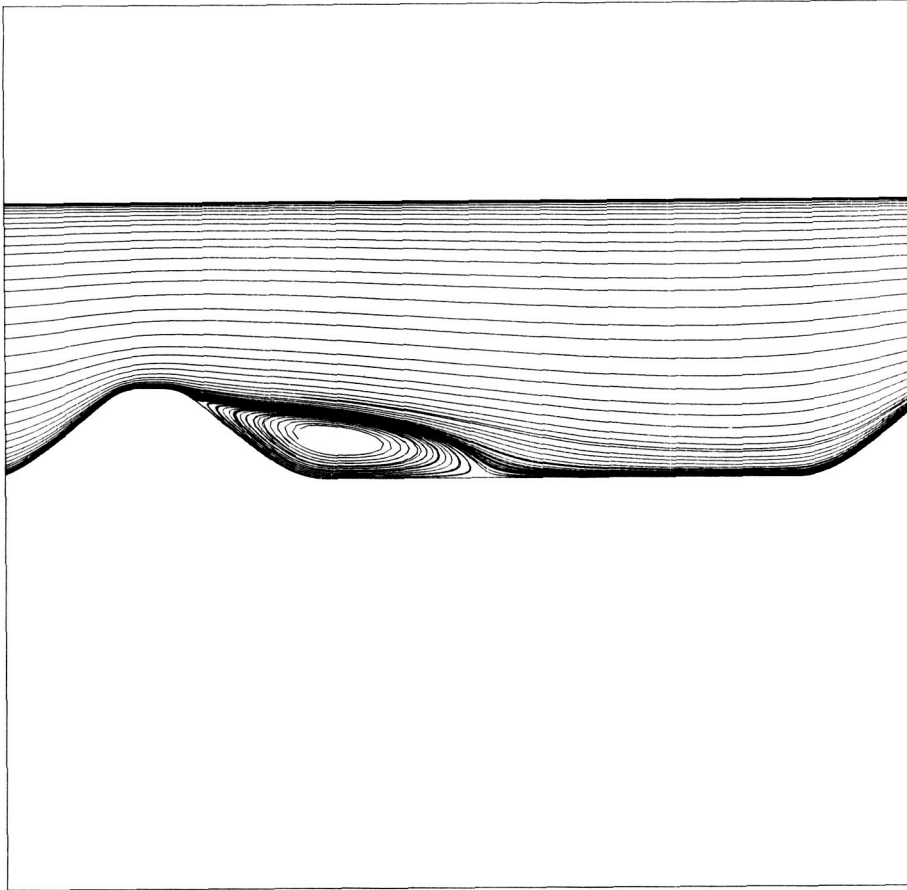


Figure 19: Streamlines for 2-D hill using EASM-ke, 737×193 grid.

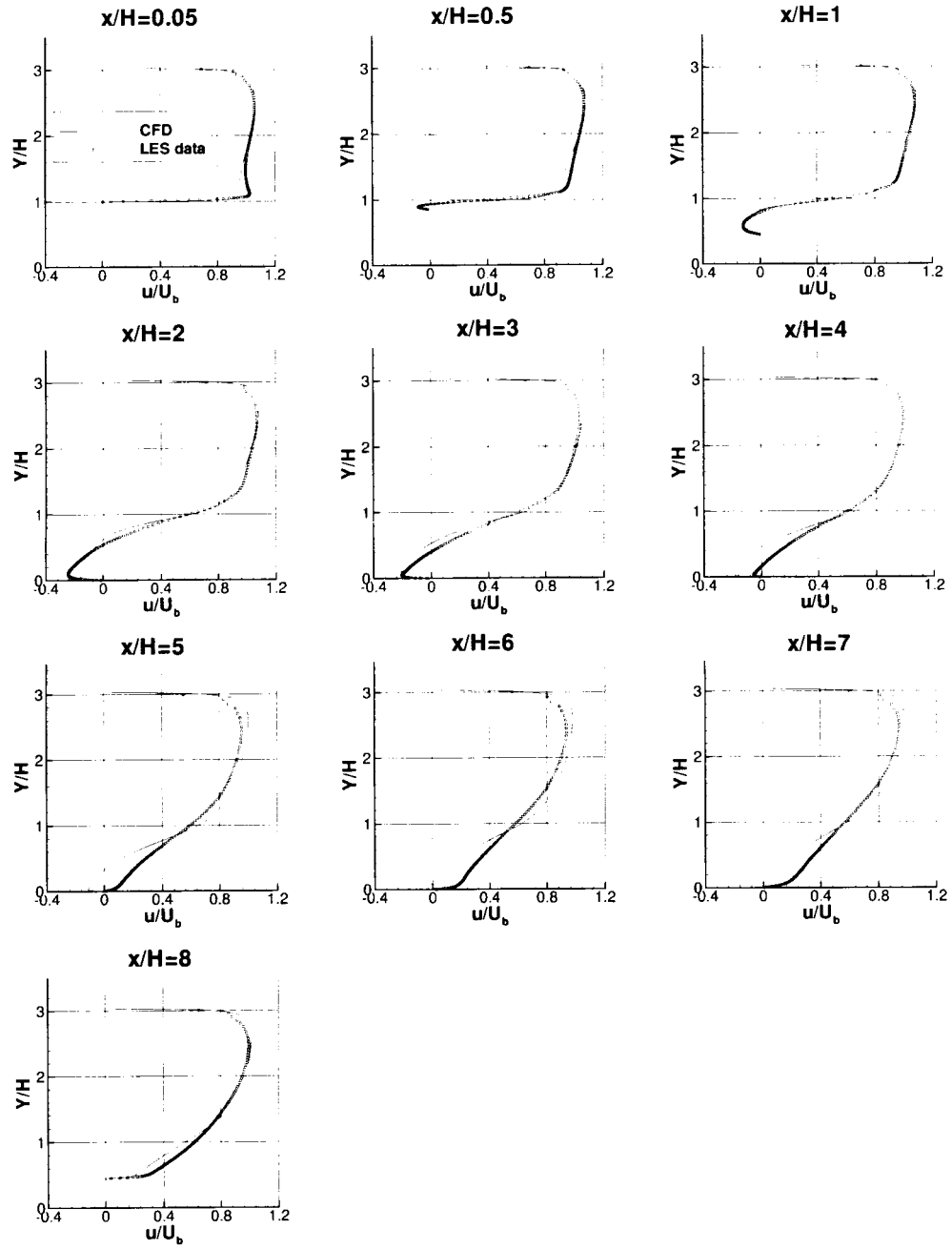


Figure 20: Velocity profiles for 2-D hill using EASM-ko, 737×193 grid.

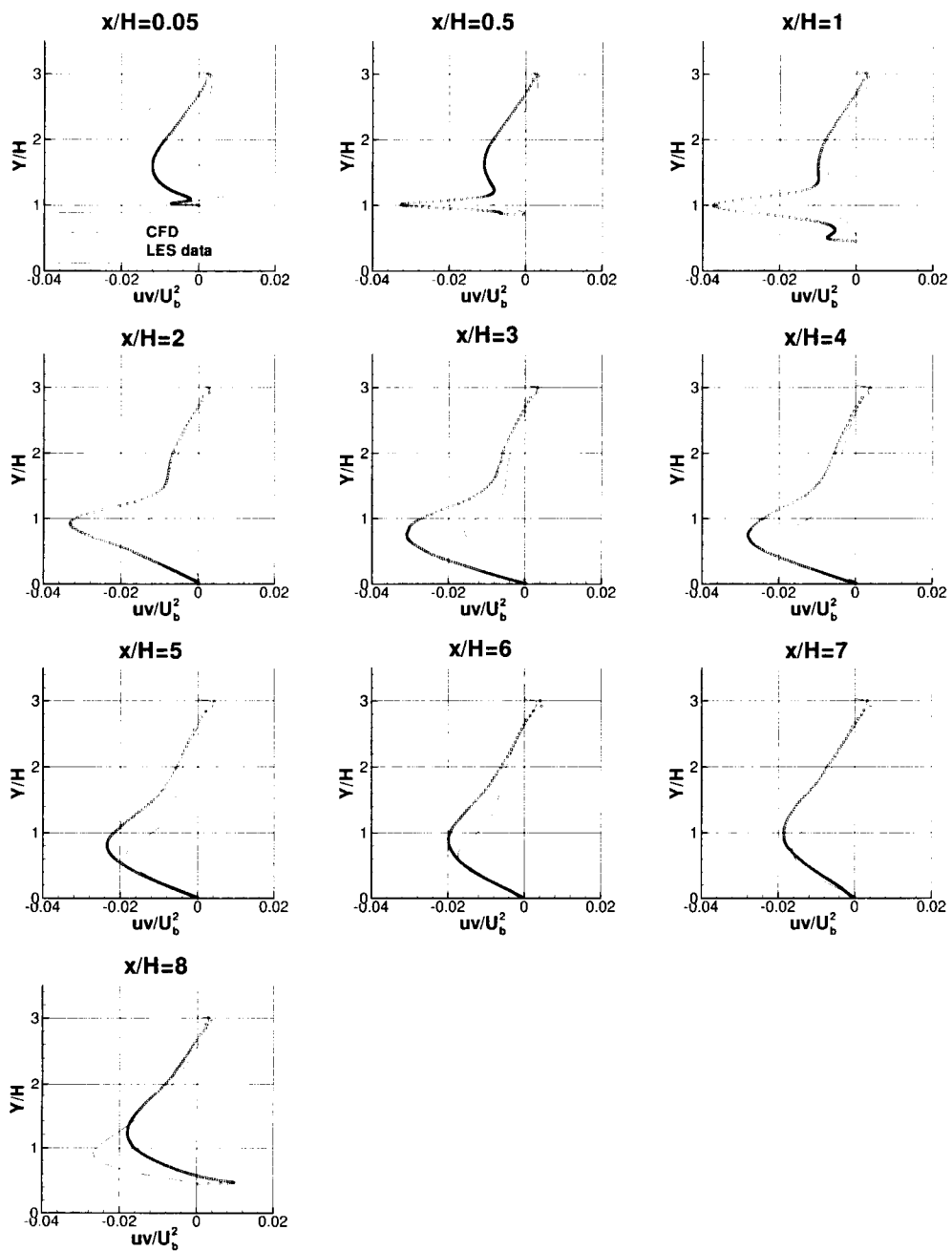


Figure 21: Turbulent shear stress profiles for 2-D hill using EASM-ko, 737 x 193 grid.

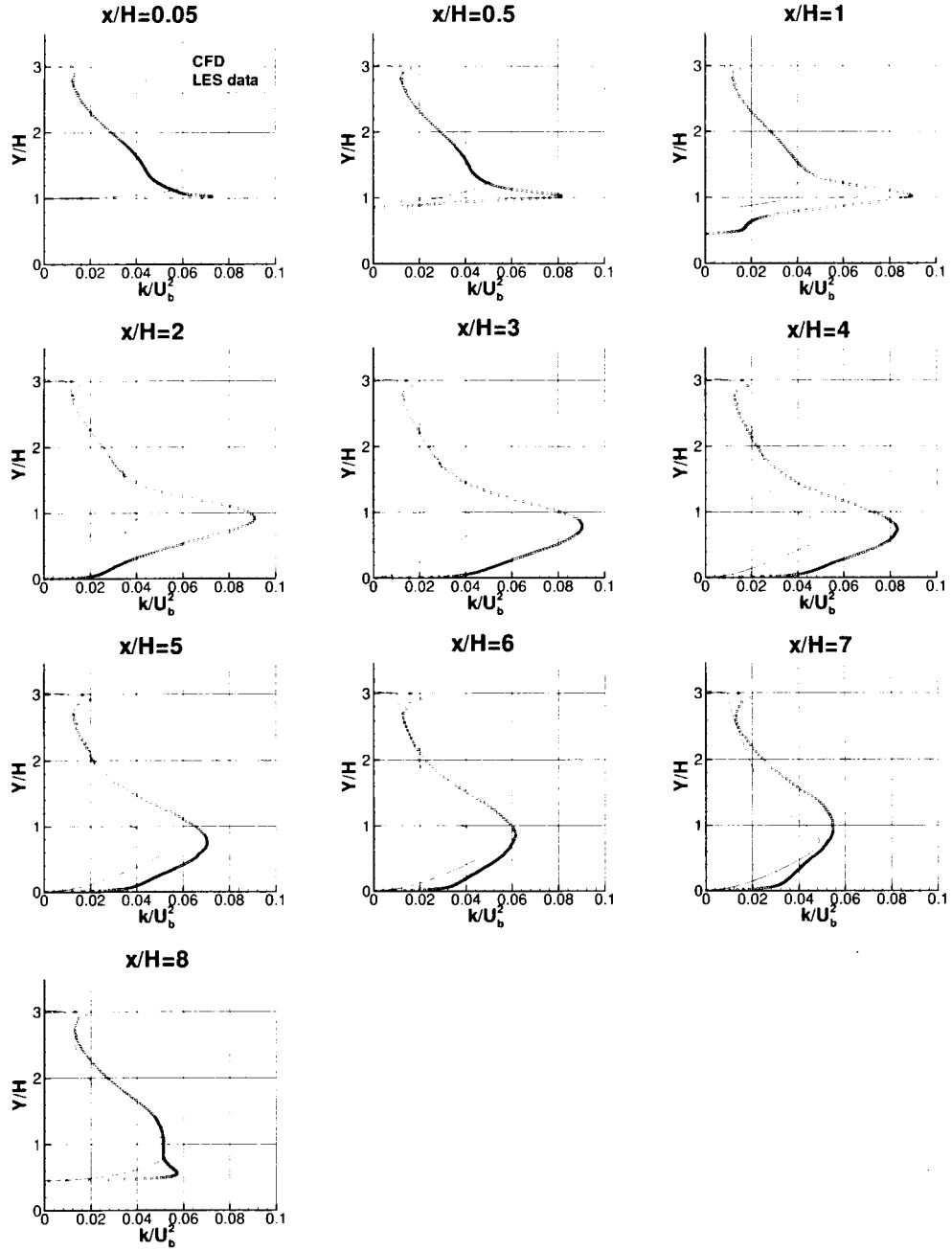


Figure 22: Turbulent kinetic energy profiles for 2-D hill using EASM-ko, 737×193 grid.

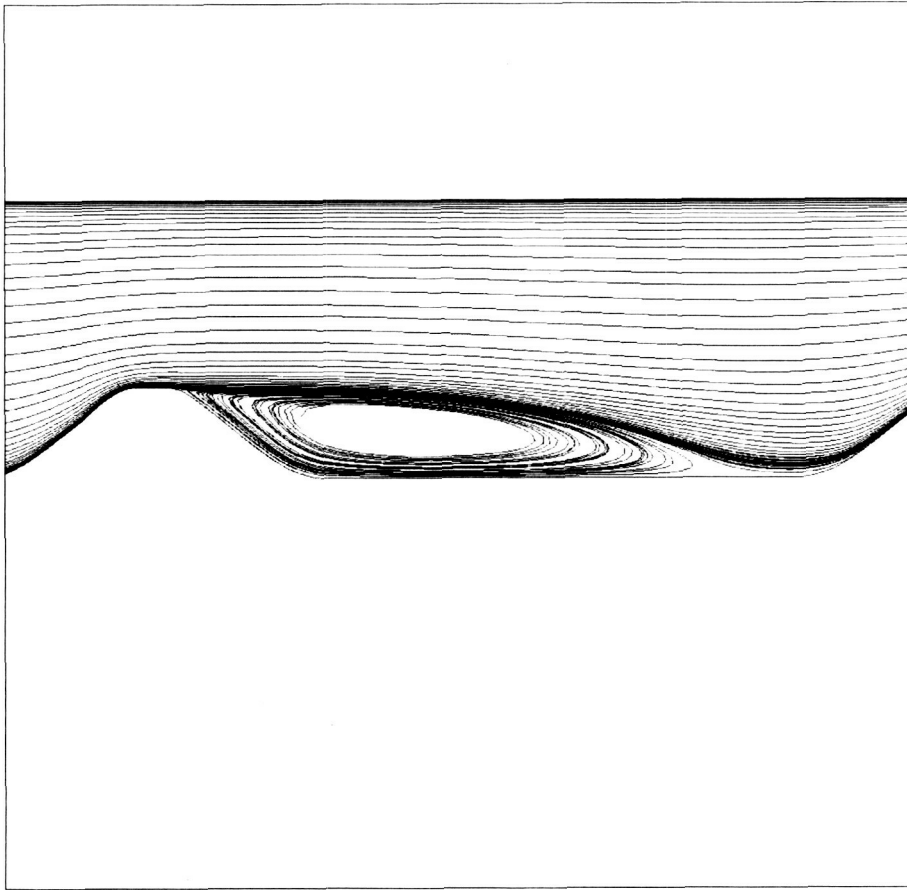


Figure 23: Streamlines for 2-D hill using EASM-ko, 737×193 grid.

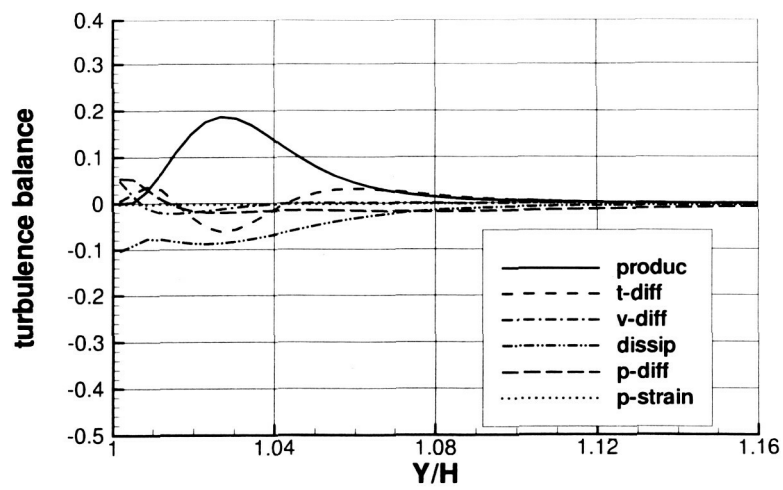


Figure 24: Turbulence budget for 2-D hill at $x/H=0.05$, LES.

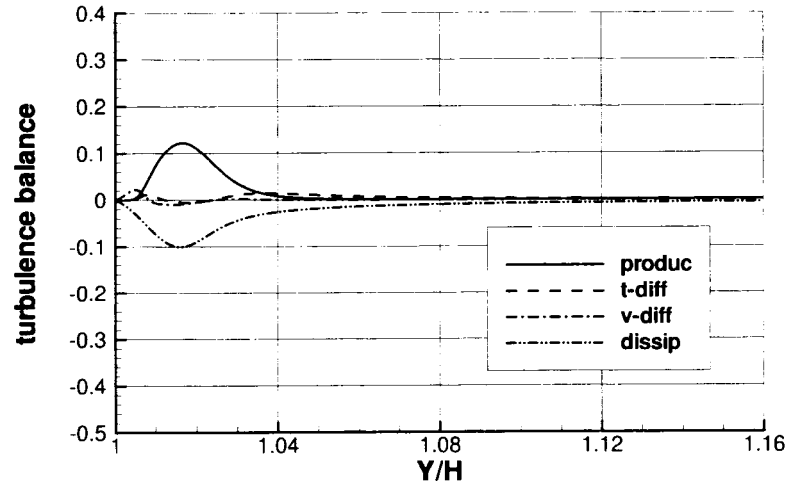


Figure 25: Turbulence budget for 2-D hill at $x/H=0.05$, using SST, 737×193 grid.

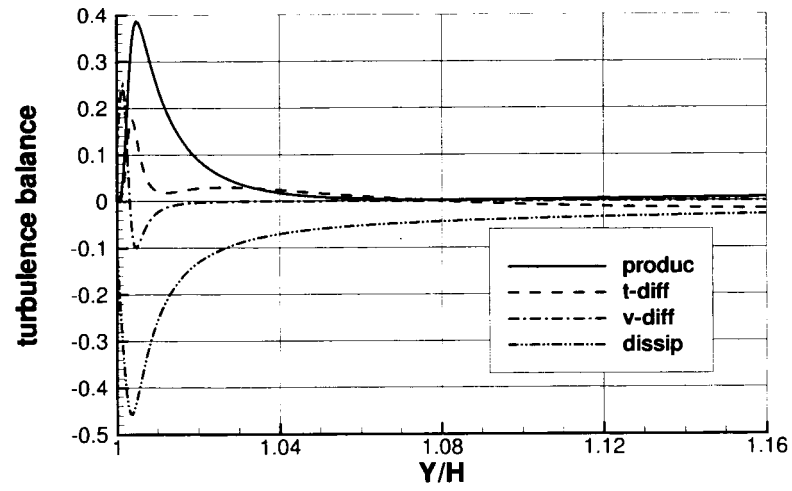


Figure 26: Turbulence budget for 2-D hill at $x/H=0.05$, using EASM-ke, 737×193 grid.

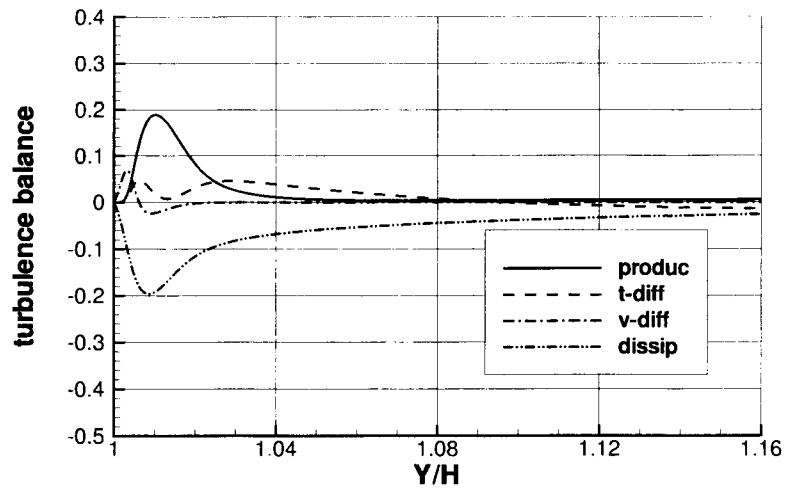


Figure 27: Turbulence budget for 2-D hill at $x/H=0.05$, using EASM-ko, 737×193 grid.

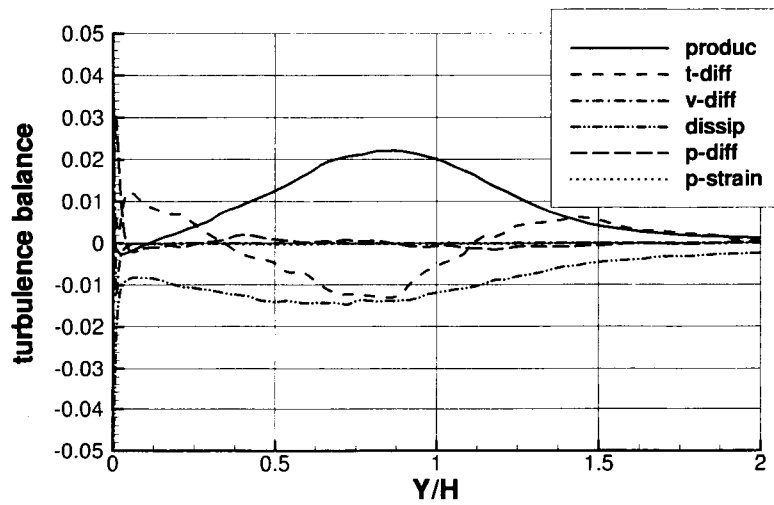


Figure 28: Turbulence budget for 2-D hill at $x/H=4$, LES.

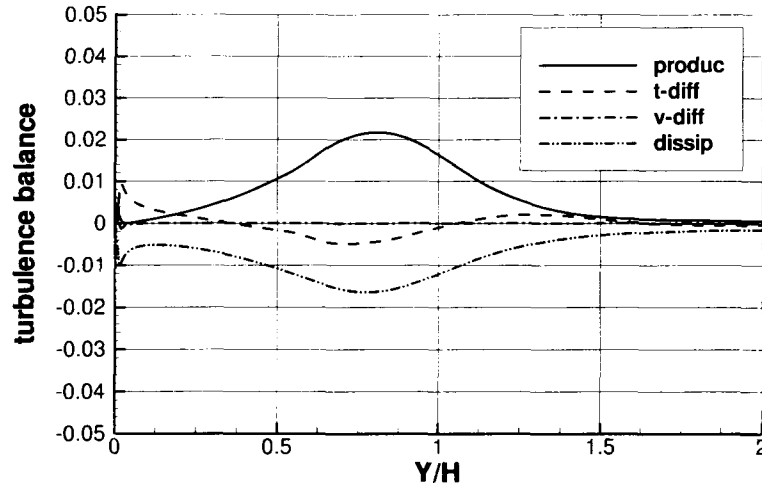


Figure 29: Turbulence budget for 2-D hill at $x/H=4$, using SST, 737×193 grid.

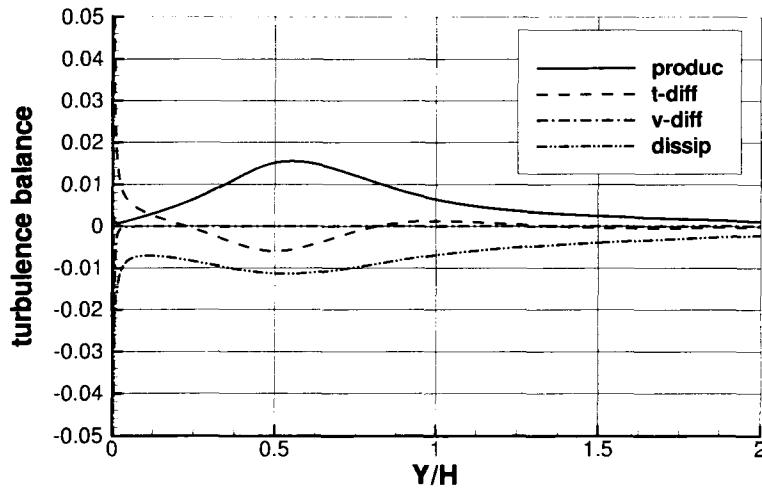


Figure 30: Turbulence budget for 2-D hill at $x/H=4$, using EASM-ke, 737×193 grid.

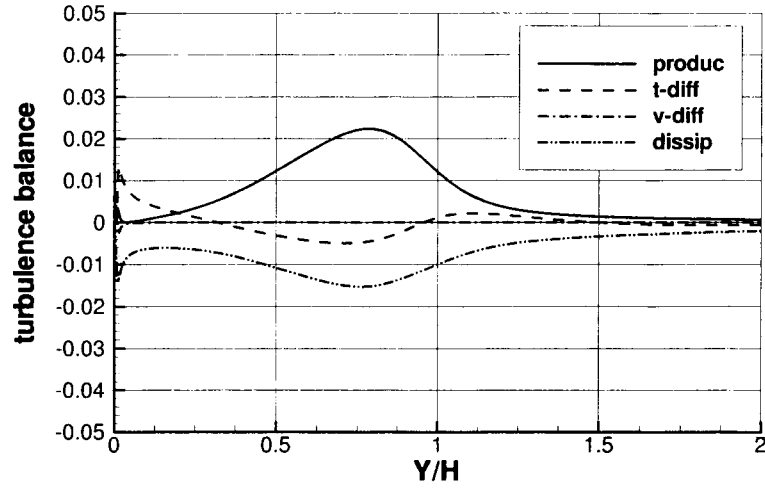


Figure 31: Turbulence budget for 2-D hill at $x/H=4$, using EASM-ko, 737×193 grid.

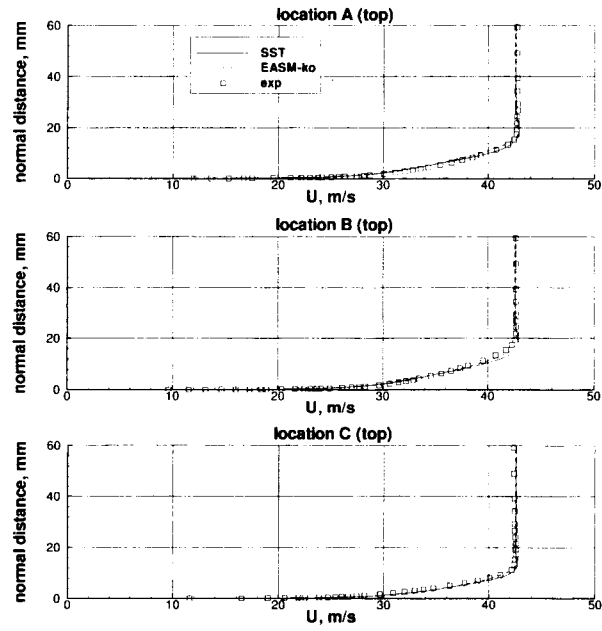


Figure 32: Central-Ahmed body u -velocity profiles on the top.

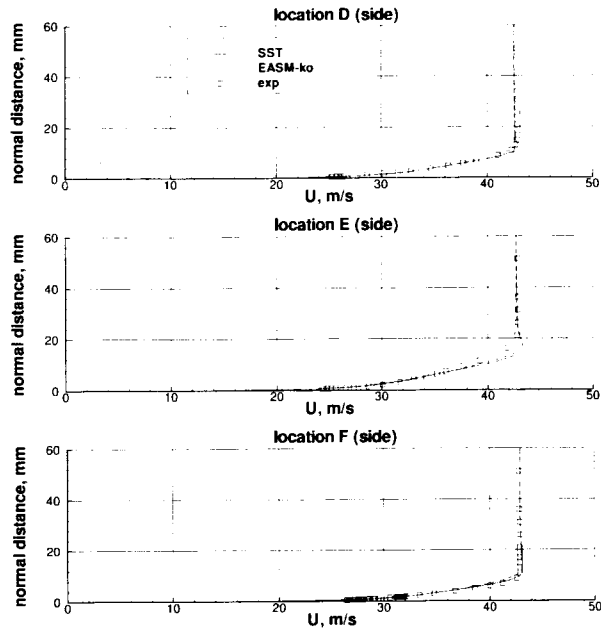


Figure 33: Central-Ahmed body u -velocity profiles on the side.

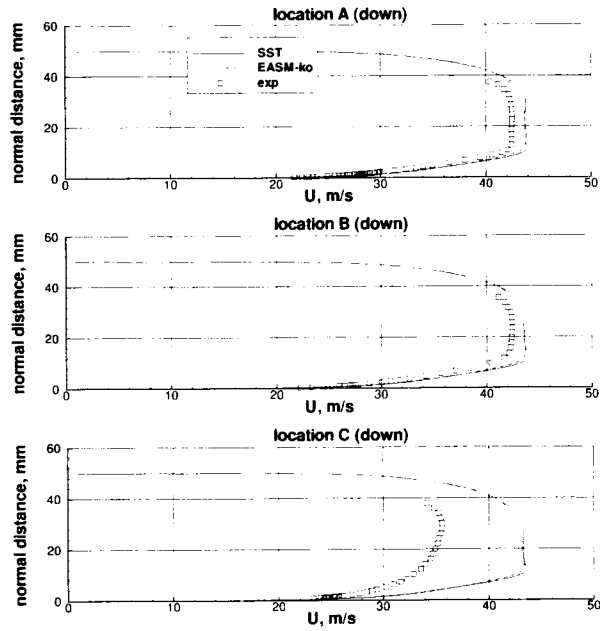


Figure 34: Central-Ahmed body u -velocity profiles on the bottom.

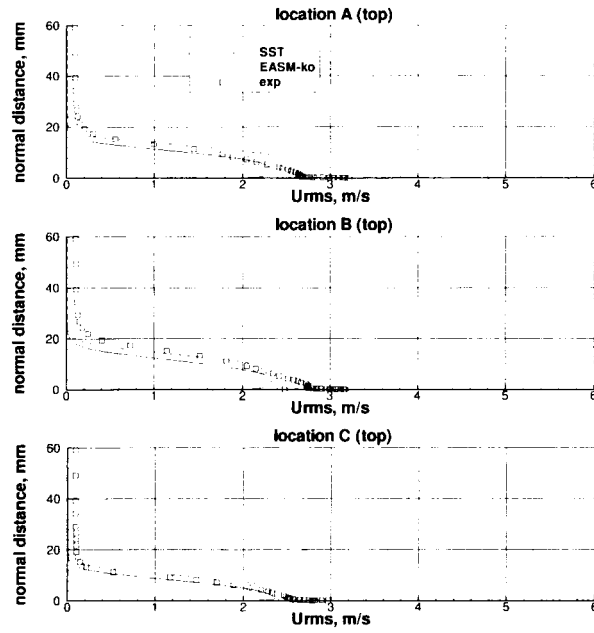


Figure 35: Central-Ahmed body U_{rms} profiles on the top.

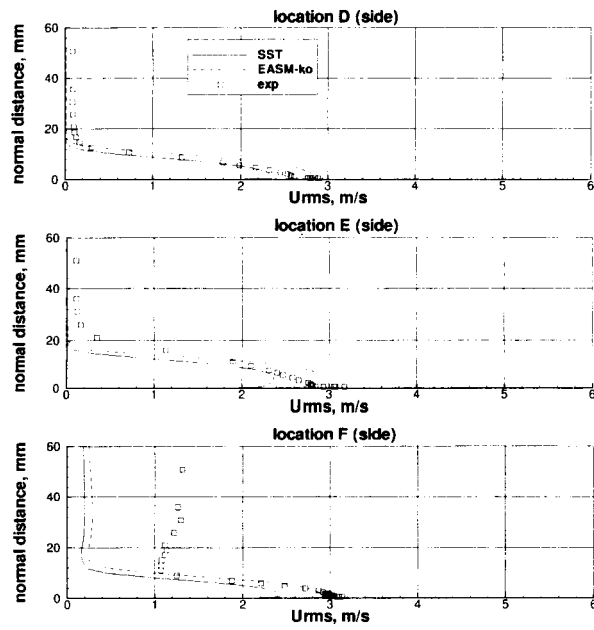


Figure 36: Central-Ahmed body U_{rms} profiles on the side.

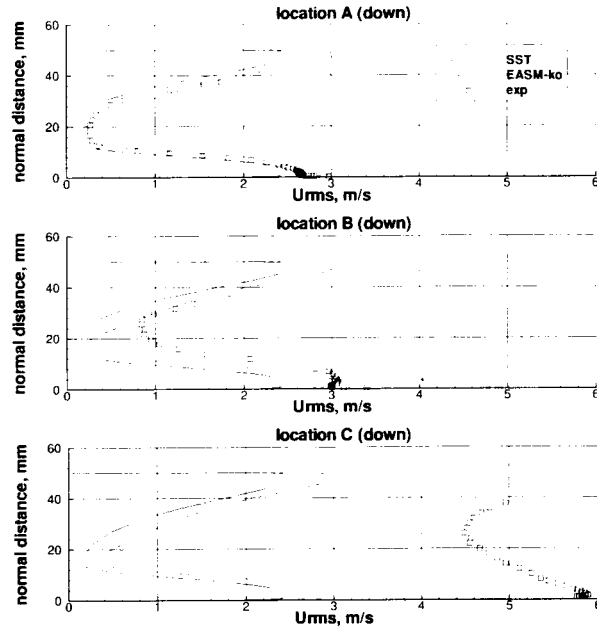


Figure 37: Central-Ahmed body U_{rms} profiles on the bottom.

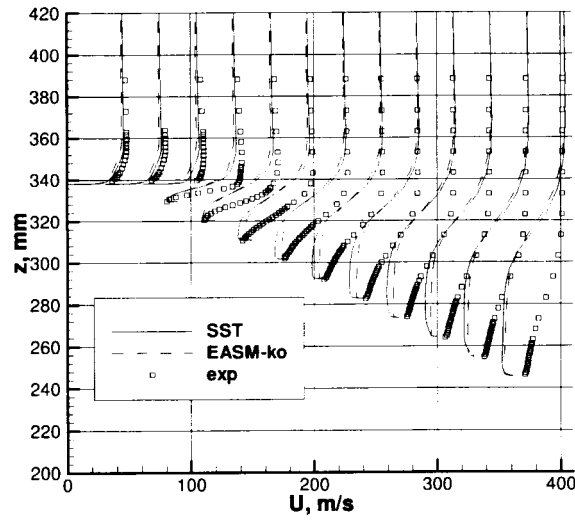


Figure 38: Profiles of u -velocity on the centerline of the 25° slant (each profile separated by 30 units in the x -direction).

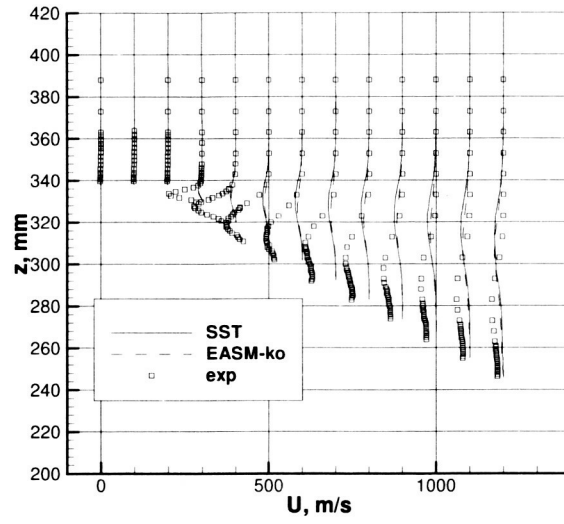


Figure 39: Profiles of $u'w'$ on the centerline of the 25° slant (each profile separated by 100 units in the x-direction).

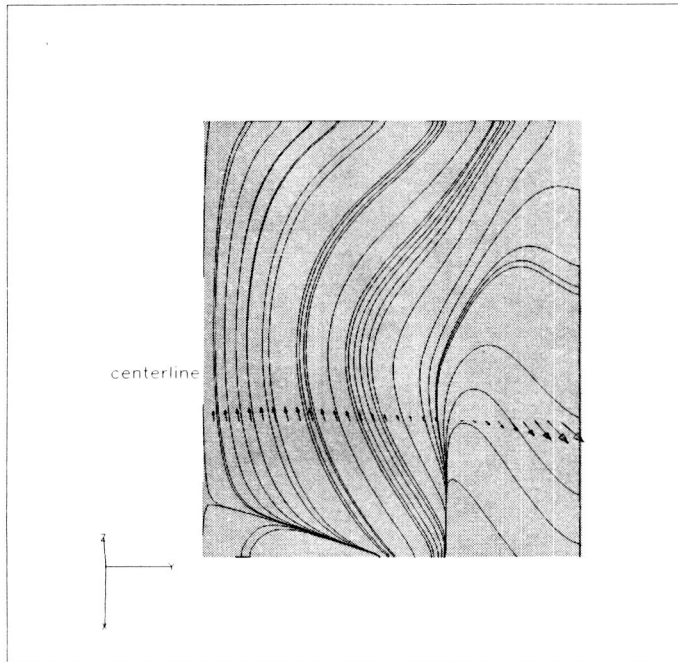


Figure 40: Streamlines on the 25° slant face, SST.

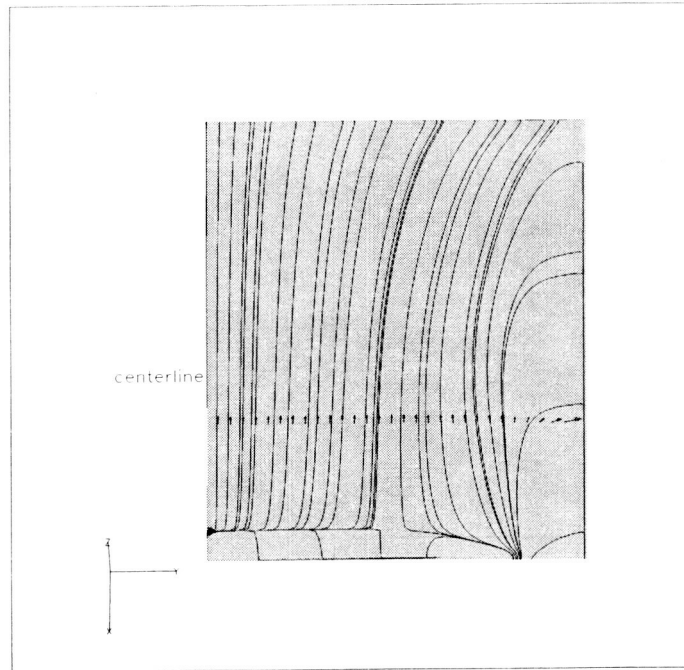


Figure 41: Streamlines on the 25° slant face, EASM-ko.

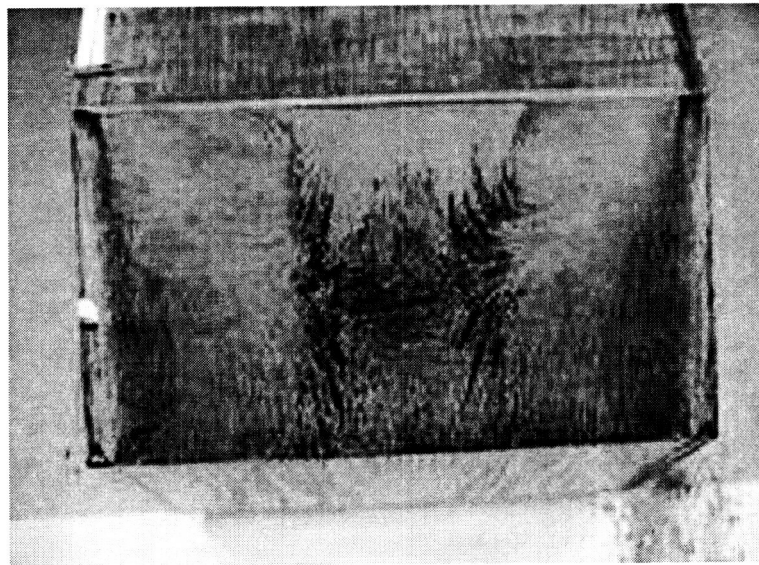


Figure 42: Oil/soot streak flow visualization on the 25° slant face, from [14].

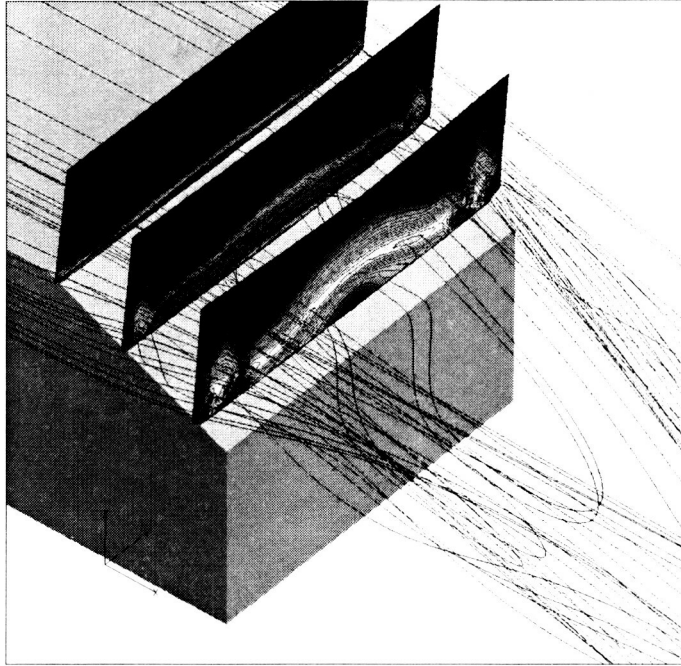


Figure 43: Vorticity contours and streamlines on the 25° slant, SST.

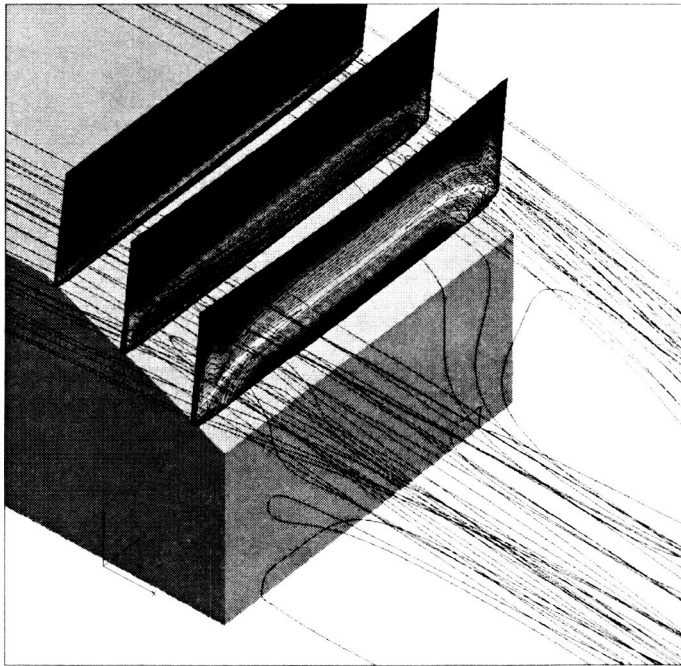


Figure 44: Vorticity contours and streamlines on the 25° slant, EASM-ko.

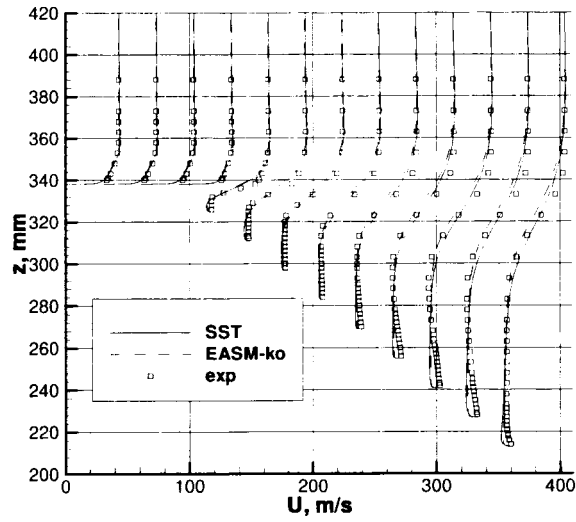


Figure 45: Profiles of u -velocity on the centerline of the 35° slant (each profile separated by 30 units in the x -direction).

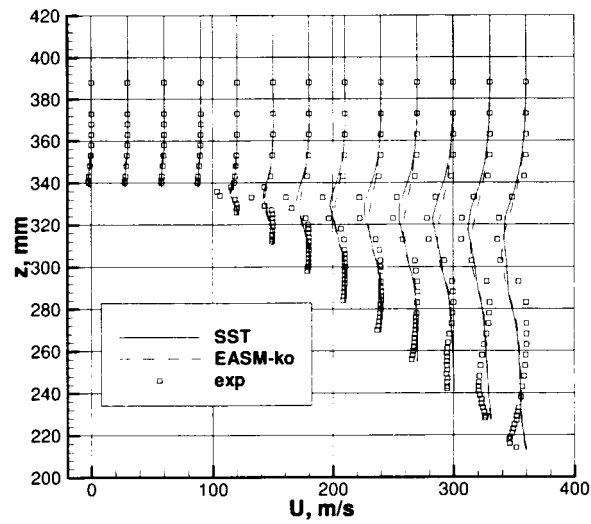


Figure 46: Profiles of $u'u'$ on the centerline of the 35° slant (each profile separated by 30 units in the x -direction).

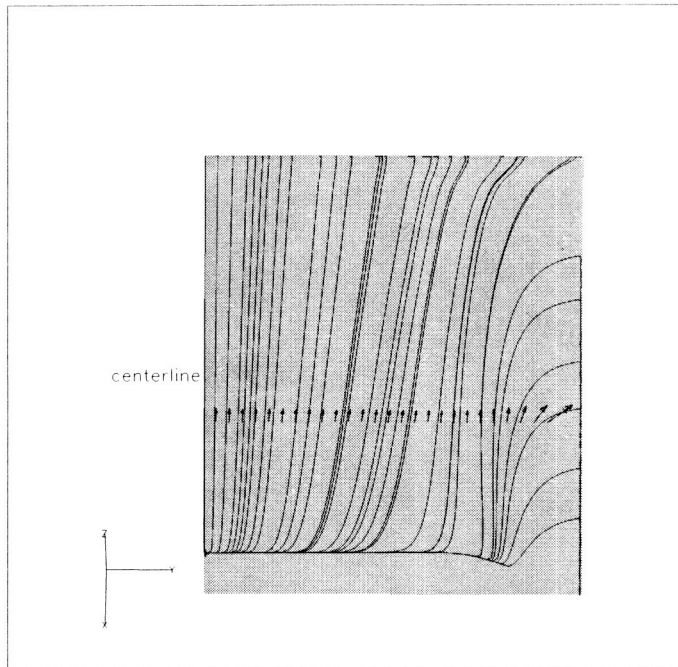


Figure 47: Streamlines on the 35° slant face, SST.

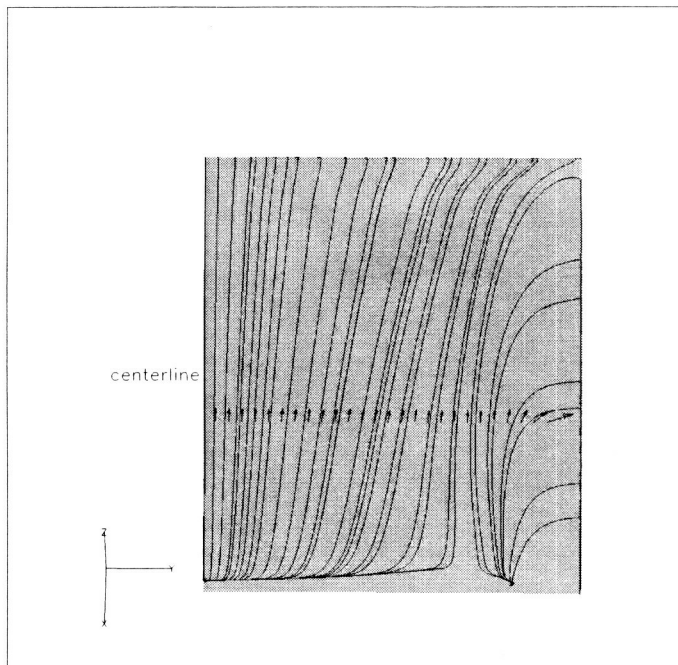


Figure 48: Streamlines on the 35° slant face, EASM-ko.

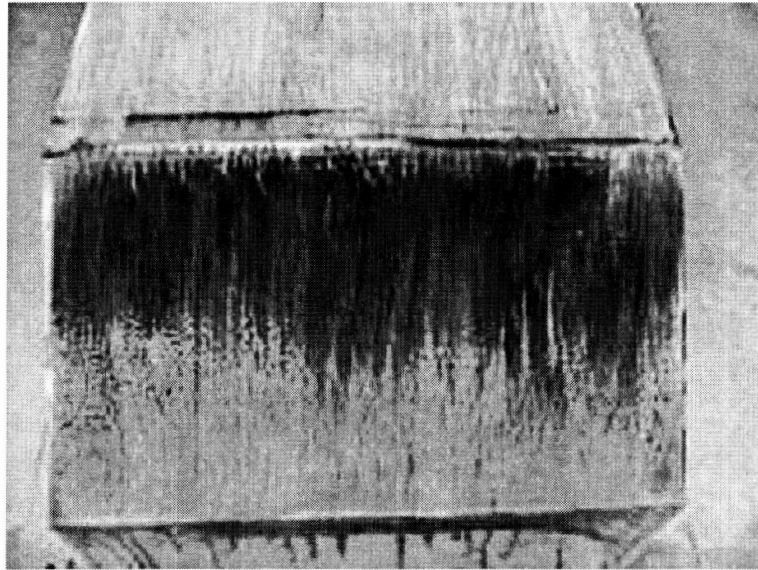


Figure 49: Oil/soot streak flow visualization on the 35° slant face, from [14].

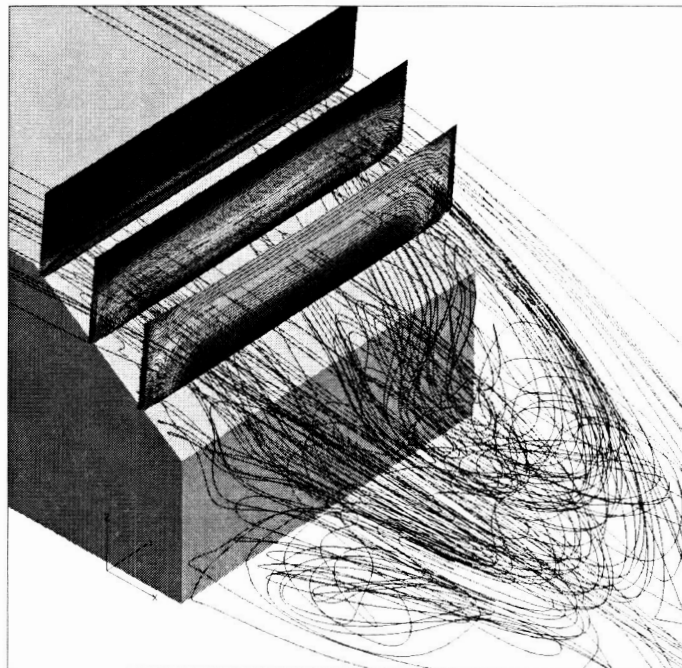


Figure 50: Vorticity contours and streamlines on the 35° slant, SST.

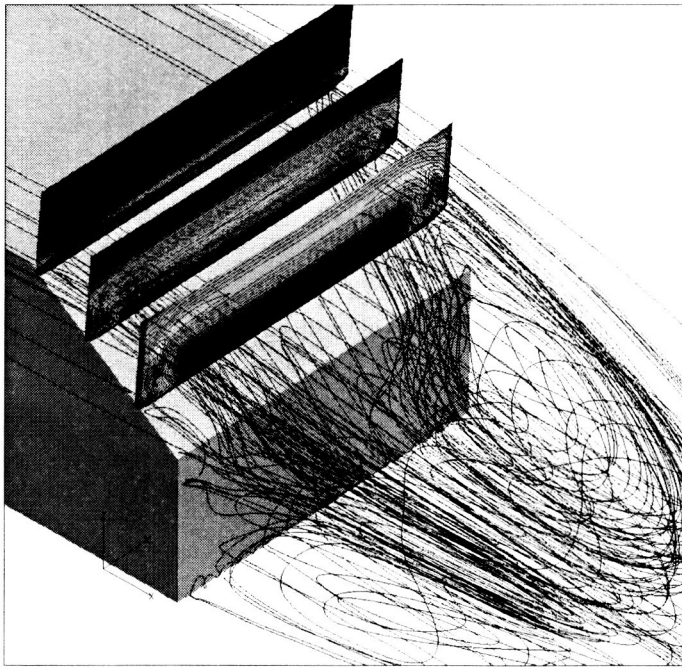


Figure 51: Vorticity contours and streamlines on the 35° slant, EASM-ko.

REPORT DOCUMENTATION PAGE			Form Approved OMB No. 0704-0188	
Public reporting burden for this collection of information is estimated to average 1 hour per response, including the time for reviewing instructions, searching existing data sources, gathering and maintaining the data needed, and completing and reviewing the collection of information. Send comments regarding this burden estimate or any other aspect of this collection of information, including suggestions for reducing this burden, to Washington Headquarters Services, Directorate for Information Operations and Reports, 1215 Jefferson Davis Highway, Suite 1204, Arlington, VA 22202-4302, and to the Office of Management and Budget, Paperwork Reduction Project (0704-0188), Washington, DC 20503.				
1. AGENCY USE ONLY (Leave blank)		2. REPORT DATE May 2003		3. REPORT TYPE AND DATES COVERED Technical Memorandum
4. TITLE AND SUBTITLE Effect of Turbulence Models on Two Massively-Separated Benchmark Flow Cases			5. FUNDING NUMBERS 762-20-11-06	
6. AUTHOR(S) Christopher L. Rumsey				
7. PERFORMING ORGANIZATION NAME(S) AND ADDRESS(ES) NASA Langley Research Center Hampton, VA 23681-2199			8. PERFORMING ORGANIZATION REPORT NUMBER L-18284	
9. SPONSORING/MONITORING AGENCY NAME(S) AND ADDRESS(ES) National Aeronautics and Space Administration Washington, DC 20546-0001			10. SPONSORING/MONITORING AGENCY REPORT NUMBER NASA/TM-2003-212412	
11. SUPPLEMENTARY NOTES				
12a. DISTRIBUTION/AVAILABILITY STATEMENT Unclassified-Unlimited Subject Category 02 Distribution: Nonstandard Availability: NASA CASI (301) 621-0390			12b. DISTRIBUTION CODE	
13. ABSTRACT (Maximum 200 words) Two massively-separated flow cases (the 2-D hill and the 3-D Ahmed body) were computed with several different turbulence models in the Reynolds-averaged Navier-Stokes code CFL3D as part of participation in a turbulence modeling workshop held in Poitiers, France in October, 2002. Overall, results were disappointing, but were consistent with results from other RANS codes and other turbulence models at the workshop. For the 2-D hill case, those turbulence models that predicted separation location accurately ended up yielding a too-long separation extent downstream. The one model that predicted a shorter separation extent in better agreement with LES data did so only by coincidence: its prediction of earlier reattachment was due to a too-late prediction of the separation location. For the Ahmed body, two slant angles were computed, and CFD performed fairly well for one of the cases (the larger slant angle). Both turbulence models tested in this case were very similar to each other. For the smaller slant angle, CFD predicted massive separation, whereas the experiment showed reattachment about half-way down the center of the face. These test cases serve as reminders that state-of-the-art CFD is currently not a reliable predictor of massively-separated flow physics, and that further validation studies in this area would be beneficial.				
14. SUBJECT TERMS Separated flow; Turbulence model; Hill; Ahmed body			15. NUMBER OF PAGES 52	
			16. PRICE CODE	
17. SECURITY CLASSIFICATION OF REPORT Unclassified	18. SECURITY CLASSIFICATION OF THIS PAGE Unclassified	19. SECURITY CLASSIFICATION OF ABSTRACT Unclassified	20. LIMITATION OF ABSTRACT UL	